

## **Outcrop scale reservoir characterisation and flow modelling of CO<sub>2</sub> injection in the tsunami and the barrier island – tidal inlet reservoirs of the Camarillas Fm. (Galve Sub-basin, Teruel, NE Spain)**

F.M.L. Veloso \*<sup>(1)</sup>, P. Frykman<sup>(2)</sup>, C.M. Nielsen<sup>(2)</sup>, A.R. Soria<sup>(1)</sup>, M.N. Melendez<sup>(3)</sup>

(1) Departamento de Ciencias de la Tierra, Universidad de Zaragoza. C/ Pedro Cerbuna 12, 50009, Zaragoza. Spain.

(2) GEUS Geological Survey of Denmark and Greenland, Department of Reservoir Geology, Ø. Voldgade 10, 1350 Copenhagen, Denmark

(3) Departamento de Estratigrafía, Universidad Complutense de Madrid. José Antonio Novais, 2; 28040, Madrid, Spain. Instituto de Geociencias (IGEO), UCM, CSIC.

\* Corresponding author: e-mail (permanent address): fe\_geo@hotmail.com. Phone: 0033 628 34 85 56.

Keywords: flow modelling, geological storage, CO<sub>2</sub> dissolution, thin reservoir, outcrop, sandstones.

### **Abstract**

The Camarillas Fm. of Lower Cretaceous (Spain) is a potentially good candidate for CO<sub>2</sub> storage because of its reservoir properties and its geographical location. In this study, we examined two sandstone bodies of the Camarillas Fm. in the province of Cuencas Mineras. This study does not examine or appraise the storage capacity of the Camarillas Fm. per se, but rather presents a low-cost approach for investigating the dynamic behaviour of sandstone bodies within the Camarillas Fm., determined at outcrop scales.

The porosity and permeability models of each sandstone body, the tsunami deposit at the bottom and the barrier island - tidal inlet deposit at the top, supplied two independent reservoir models reflecting different sedimentary processes. The injection rate per day (maximum 200 and 400 sm<sup>3</sup>/day) and the total amount of injected CO<sub>2</sub> (maximum of 116,000 sm<sup>3</sup>, ~200 t) were very low in comparison with an industrial site. Despite of the relative low average permeability measured from plugs (0.1–20 mD), both can serve as a reservoir and stored 50-60% of injected CO<sub>2</sub> by residual and dissolution trapping over 7.5 years. The total volume of CO<sub>2</sub> as gas phase in the reservoir (140-240 m<sup>3</sup>) at the end of simulation represented less than 1% of reservoir volume. The dissolution of CO<sub>2</sub> reached 40% of total injected CO<sub>2</sub>, where the injection point was in zones of 1–3 m-thick. The cases with the injector well located in zones of 6-7 m-thick, the CO<sub>2</sub> dissolution was 16-19%. The injection using a lower but constant and invariable flow rate without break slightly improved the CO<sub>2</sub> storage (dissolution and residual trapping), principally in cases with the injection in thicker zones, where 4% more CO<sub>2</sub> was stored. At the scale of this study (sub-metric), the

thickness of reservoir has great impact on the amount of CO<sub>2</sub> dissolution in the zone close to the injector well.

## 1. Introduction

The 'greenhouse effect' refers to processes that trap heat in the atmosphere and thus prevent heat loss to space. The effect is primarily the result of enhanced concentrations of carbon dioxide (CO<sub>2</sub>) and other gases in the atmosphere that absorb and re-radiate energy. Human activity related to the burning of fossil fuels is largely responsible for recent changes in the natural CO<sub>2</sub> balance of the Earth–atmosphere system, and is thus responsible for the recent intensification of the greenhouse effect on Earth (IEA-GHG, 2013). In Europe alone, the total emission of CO<sub>2</sub> from the 28 member states (EU28) caused by human activity (excluding land use activities and land-use changes and forestry; LULUCF) was 2.99 billion tonnes in 2012. The main source of CO<sub>2</sub> emissions was public electricity and heat production (PEHP), which correspond to 27% of the total CO<sub>2</sub> emission. Spain was responsible for 7.5% of the European CO<sub>2</sub> emission, occupying 7th place in terms of emissions after Poland (EEA, 2015).

Carbon dioxide capture and geological storage (CCS) is a bridging technology that will contribute to the mitigation of climate change, as it reduces the amount of CO<sub>2</sub> in the atmosphere. The CCS strategy consists of capturing CO<sub>2</sub> from industrial emissions and transporting it to storage sites for injection into suitable underground geological formations for permanent storage. However, the characterization and selection of appropriate CCS sites is a lengthy and costly process, and so must begin early in the project planning process. Geological storage of CO<sub>2</sub> requires satisfactory characterization of reservoir and caprock geology at both local and regional scales, to elucidate CO<sub>2</sub> migration patterns and overall storage potential. The characterization and assessment of potential storage sites is based on dynamic modelling comprising a variety of time-step simulations of CO<sub>2</sub> injection into the storage site, using three-dimensional static geological Earth models and a complex computerized storage simulator (EU, 2009).

Site selection for geological storage of CO<sub>2</sub> is a complex issue involving a variety of geological and non-geological variables. The quality of the reservoir rocks and the seal system are of particular importance in site selection, as is the proximity of the site to CO<sub>2</sub> emission sources. The Camarillas Fm. of Lower Cretaceous (Spain) is a potentially good candidate for CO<sub>2</sub> storage because of its sedimentological characteristics (Navarrete, 2015), reservoir properties and geographical location (Fig. 1). The Camarillas Fm. is located in the province of Cuencas Mineras, which has been one of the most important regions in Spain for the supply of raw materials, such as coal, iron and gypsum, and for the generation of electricity from coal-fired power stations through the centuries. Today, the Andorra power plant, located 60 km from the study area, is one of the most important heat and electricity generation facilities in the Spain. A large-scale study of the potential of the Camarillas Fm. for CO<sub>2</sub> storage would be costly and prolonged; consequently, this study does not examine

or appraise the storage capacity of the Camarillas Fm. per se, but rather presents a low-cost approach for investigating the dynamic behaviour of two sandstone units within the Camarillas Fm., determined at the outcrop scale.

In this study, we examined two sandstones bodies of the Camarillas Fm at the Aliaga outcrop. The study of the outcrop at sub-metric scale for 200 m-long, supplied two independent reservoir models reflecting different sedimentary processes. The petrophysical models of the tsunami and barrier island –tidal inlet (b.i./inlet) deposits were converted to reservoir models for simulation study of CO<sub>2</sub> injection. The size of reservoir models represent here nearly one grid block (grid cell) of classic reservoir models. The complexity of tsunami and b.i./inlet models is related to the grid resolution (size and number of grid blocks) and the petrophysics distribution in the reservoir.

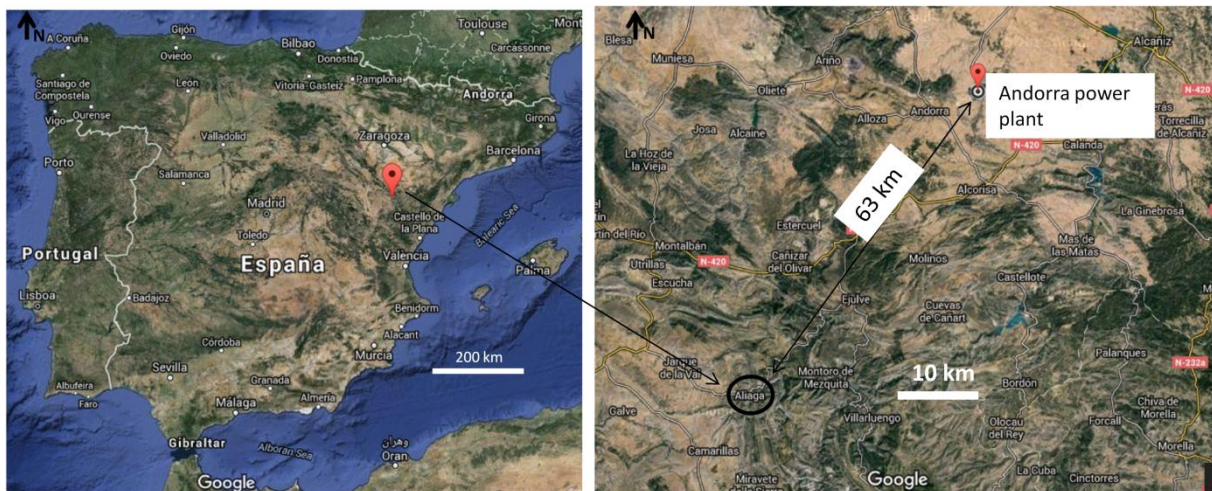


**Fig. 1: Location map of case study in the Aliaga village and the Andorre power plant.**

Reservoir modelling is essential in studies of geological storage of the CO<sub>2</sub> to understand the behaviour of CO<sub>2</sub> in the reservoir for a safely and efficiently storage. The reservoir model is a petrophysical model reflecting the rock heterogeneity which can potentially influence the CO<sub>2</sub> migration in the reservoir through different time scales (Fig. 2). The petrophysical model and its architecture are of course important, but also the fluid model and its physical and chemical properties which lead the processes of CO<sub>2</sub> trapping (Fig. 2) and movement. Buoyancy forces are the most important mechanism driving the CO<sub>2</sub> movement in the reservoir by the difference of density (IPCC, 2005; Frykman, 2009).

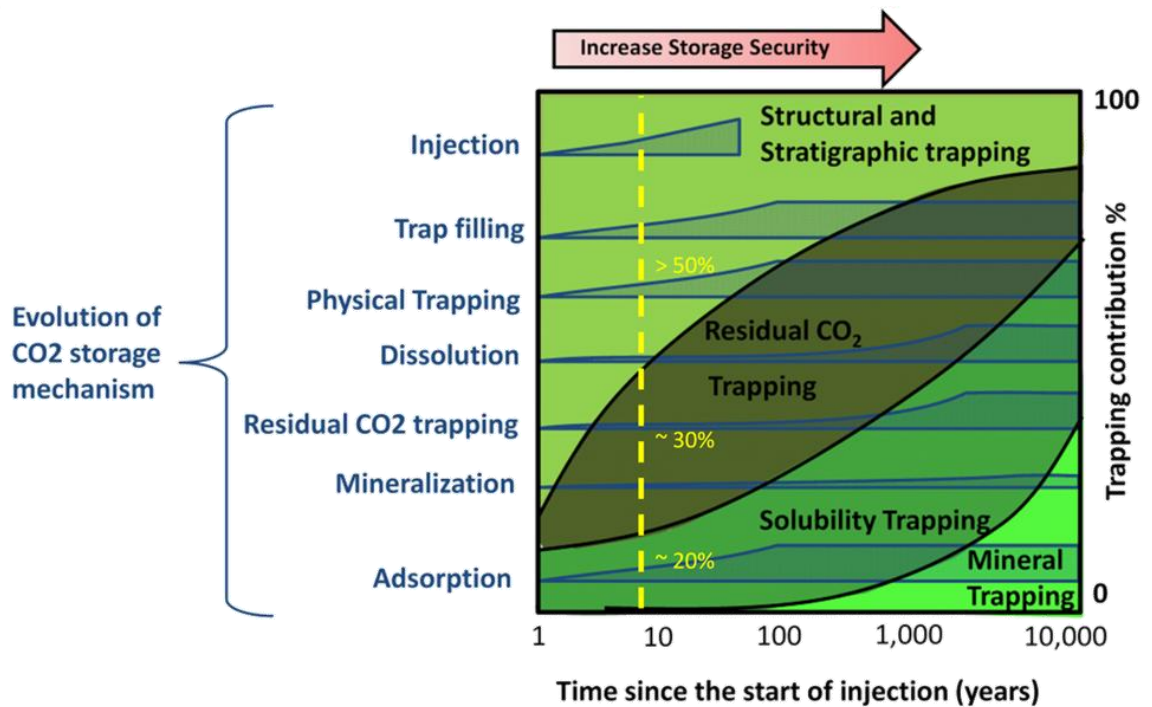


**Fig. 2: Evolution of CO<sub>2</sub> storage mechanisms through time. The horizontal axis shows the time since the start of injection; the right vertical axis shows the trapping contribution percentage of the four main storage mechanisms; the left vertical axis shows the qualitative evolution of CO<sub>2</sub> storage mechanisms. The dashed line represents the simulation time of this study and the percentage contribution of the CO<sub>2</sub> storage mechanisms. Modified from IPCC (2005).**

The physical and chemical properties of components of the fluid model and its evolution with pressure and temperature, principally of the CO<sub>2</sub> component, determine the behaviour and trapping mechanism of injected CO<sub>2</sub> and its evolution in the reservoir during and after the injection operation (Fig. 2). Four main trapping mechanisms (Fig. 2) allowed permanent and safe CO<sub>2</sub> storage in reservoir rocks (IPCC, 2005; Chadwick *et al.*, 2008). (1) Structural and stratigraphic trapping: CO<sub>2</sub> is physically trapped by low-permeability and low-diffusivity top-seal rocks. (2) Residual saturation trapping: capillary forces and adsorption onto surfaces of mineral grains in the rock matrix immobilise a proportion of the injected CO<sub>2</sub> as residual CO<sub>2</sub> gas phase. (3) Dissolution trapping: dissolution of injected CO<sub>2</sub> in reservoir brine. (4) Geochemical trapping: reaction of dissolved CO<sub>2</sub> with native pore fluids and/or minerals constituting of the rock matrix.

The dissolution of CO<sub>2</sub> in brine is one of the most important mechanism for safe long-term entrapment of CO<sub>2</sub> (IPCC, 2005); the dissolved CO<sub>2</sub> may, over thousands of years, be converted to stable carbonate minerals, thus trapping the CO<sub>2</sub> as mineral phase in the reservoir (Fig. 2). The CO<sub>2</sub> as a mobile gas in the reservoir moves upwards driven by buoyancy; this phenomena increases the risk of leakage (IEA-GHG, 2009) by diffusion across caprock formations, mobilization through natural faults and fractures, and through human-made features such as wellbores (Celia *et al.*, 2005). Leakage types range from short-term large leakage to long-term diffuse leakage (Chadwick *et al.*, 2008). Although the CO<sub>2</sub> trapped

by residual saturation is effectively immobile, an upwards leakage pathway may degas CO<sub>2</sub> as saturated brine is depressurized (IPCC, 2005); when CO<sub>2</sub> is dissolved it no longer exists as a separate phase, thereby eliminating the buoyant forces that drive it upwards (IPCC, 2005).

Geological storage of CO<sub>2</sub> can be undertaken in a variety of geological settings in sedimentary basins: oil fields, depleted gas fields, deep coal seams and saline formations are all possible storage formations (IPCC, 2005). Some studies have shown that storage in saline formations has the greatest potential, with an estimated storage capacity of 1,000–10,000 Gt (IPCC, 2005; IEA-GHG, 2013). Thus, the scenario of flow simulation of this study is a deep saline aquifer. Four study cases in each reservoir, the tsunami and the barrier island – tidal inlet, tested the sensibility of the location of injector well and the thickness of the reservoir in the behaviour of injected CO<sub>2</sub> during a short-injection and pos-injection period. The simulation studies of CO<sub>2</sub> injection were undertaken in Eclipse 300 (E300) software (courtesy of Schlumberger) using the CO2STORE option.

## 2. Reservoir model

The facies and petrophysical modelling of the tsunami and the barrier island – tidal inlet (b.i./inlet) deposits were performed using Petrel software (courtesy of Schlumberger). The Aliaga outcrop was divided into two sectors, the North sector and the South sector, separated by the TEV8008, the Aliaga–Miravete road; the tsunami facies (Navarrete *et al.*, 2014) at the bottom and the barrier island/tidal inlet facies (Navarrete *et al.*, 2013) at the top of the outcrop profile (Fig. 3). Samples were collected at regularly spaced intervals along the two sandstone bodies. In areas where such deposits are thicker than 1 m, several samples were collected, which were located at the base, middle and top of each bed. Samples were extracted using a portable rock core drill. Orientations of the extracted cores were measured; their dimensions varied from 10 to 20 cm in length and 8 to 9.5 cm in diameter. The cores were obtained parallel to the dip direction, and were taken on the outcrop face due to constraints imposed by the steeply dipping orientation of the sedimentary layers in the outcrop (Veloso *et al.*, 2013). Samples were taken from each core for petrographic and petrophysical analyses.



**Fig. 3: Aerial photograph of Aliaga outcrop, supplied by the Aragon Visor 2D (<http://sitar.aragon.es/>) with the location of the Tsunami deposit and barrier-island and inlet deposit,**

The petrophysical measurements included estimations of sample porosity and permeability by direct measurements on plugs. Fifty-six plugs were taken from the cores for measurements of porosity ( $\Phi$ ) and horizontal permeability ( $K_h$ ); a further 23 plugs were used for measurements of vertical permeability ( $K_v$ ). The petrophysical measurements were conducted at the Petrophysics Institute Foundation (IPF) of Madrid, Spain, on plugs 60 mm long and 40 mm in diameter. The plugs were cut from the cores as shown in Fig. 4, where the vertical plugs were taken perpendicular to the strike direction or the North direction, and the horizontal plugs were taken parallel to the strike direction or the North direction. Porosity was estimated by a helium pycnometer at atmospheric conditions and ambient temperatures through gas displacement inside a known cell volume; the pore volume was obtained according to Boley's law (IPF, 2012). The horizontal ( $K_h$ ) and vertical ( $K_v$ ) permeabilities were estimated using a gas permeameter at steady-state conditions; the gas permeability was calculated according to Darcy's law and was then corrected to the equivalent liquid permeability using the Klinkenberg correction factor (IPF, 2012).

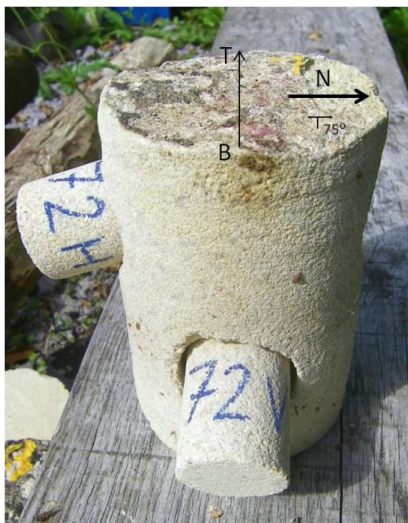


**Fig. 4: Schema for obtaining plugs for petrophysical measurements. The core length is equal to the width of deposit; "V" plugs were used to measure the vertical permeability and "H" plugs were used to measure the horizontal permeability; "T" and "B" correspond to the top and base of bedding; respectively.**

Lithofacies described in the field were refined by petrographic descriptions of 65 thin sections, which were made from samples collected from core and hand specimens. Thin sections were oriented perpendicular to bedding, and were chemically stained to identify carbonate. The classification used for the mineralogical analyses was based on that of Pettijohn (1973). Veloso *et al.* (2016) classified lithofacies as function of sand sorting and cement content. The analysis showed the good correlation between facies and petrophysics distributions, principally in the b.i./inlet deposit.

The porosity and permeability models of deposits, the tsunami and the b.i./inlet, supplied two reservoir models; their dimensions are given in Table 1. The b.i./inlet reservoir has 199,818 active grid blocks between layers K 1 (top) – 30 (base) and the tsunami reservoir has 92,659 active grid blocks between layers K 33 (top) - 42 (base).

**Table 1: 3D grid dimensions of each reservoir model.**

Reservoirs	Horizontal j North-South	Horizontal i East-West	Vertical thickness k
B.i./inlet grid blocks	420	40	30
B.i./inlet metres	210	40	7
Tsunami grid blocks	420	40	10
Tsunami metres	210	40	3
Average size of grid block (meters)	0.5	1	0.21

## 2.1. TSUNAMI RESERVOIR MODEL

The tsunami deposit has a homogenous distribution of facies with 70% of the samples belonging to the Well sorted (WSs) and Moderate sorted (MSs) sandstones, independent of the great variation in grain size (Veloso *et al.*, 2016). The tsunami porosity (Fig. 5) ranges from 14% to 22%, with three values < 11%, and the permeability values range from 4 mD to 20 mD, with one value < 1mD. The correlation of porosity (Phi) and horizontal permeability (Kh) of measured samples can be approximated with a linear relation. Despite of the cementation in some samples, the Phi and Kh values lie within a narrow range, which is represented by ellipse in Fig. 5.

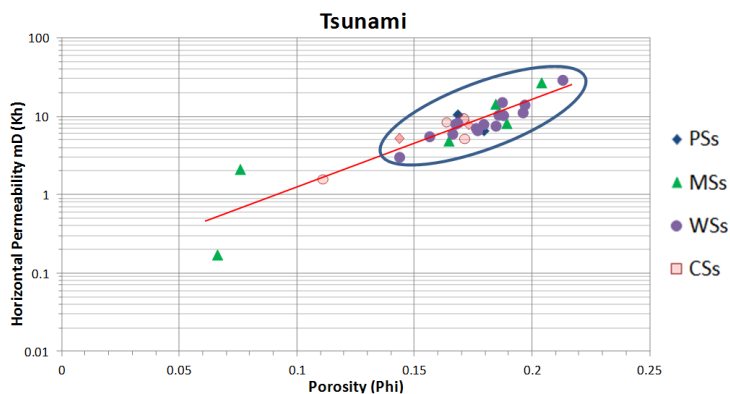


**Fig. 5: Phi versus Kh plot for the tsunami samples, classified by sorting and cemented facies. Except for three samples, the porosity values lie in the range 0.14–0.22 m<sup>3</sup>/m<sup>3</sup> (blue ellipse). The correlation between data is represented by regression function (line). The cemented samples (CSs class) are shown by pale red symbols with the point shape representing the sub-classification of sample, which is according to their sand sorting.**

The porosity modelling of tsunami deposit conditioned by facies was discarded because no real relationship was observed between porosity and sorting facies which leads to distinguishable flow properties (Pyrzcz and Deutsch, 2014). The tsunami porosity was distributed in the grid using a Gaussian algorithm, which assigns data to the nearest grid node, and then determines a random path through all grid nodes by finding nearby data and

previously simulated grid nodes, to build the conditional distribution by Kriging. The conditional distribution is based on probability distribution (Fig. 6) and semi-variograms derived from the measured porosity data (Veloso, 2015). The arithmetic mean of 17% and the standard deviation of 3% (Table 2) show the low variation of range of the measured values, with few extreme low values denoted by the variance coefficient. The minimum value of the input distribution was slightly modified to adjust the normal distribution of data (Fig. 6), consequently the arithmetic mean of modelled distribution increased a little (~1.5%), the standard deviation unchanged and the coefficient of variance decreased (Table 2).

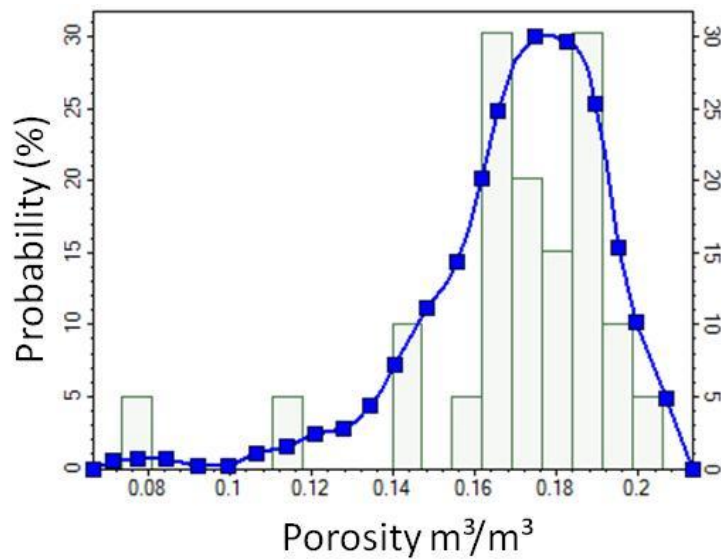


**Fig. 6: Histogram of porosity values (bars) for the Tsunami deposit. The blue curve is the adjusted normal distribution of data used in the Gaussian porosity modelling.**

**Table 2: Main statistics of porosity values for the tsunami deposit.**

Tsunami	Measured	Modelled
Number of values	30	92715
Mean	0.166	0.18
Standard deviation	0.03	0.03
coefficient of variance	0.20	0.16
Min	0.02	0.07
Max	0.2175	0.21

The Tsunami porosity model from the East and bottom perspectives, illustrated in Fig. 7A and B, respectively, shows higher (>20%) and lower (<8%) porosity values in specific zones. The layer-by-layer evolution of porosity in the model, presented in Fig. 8, shows lower values arranged as individual patches with thicknesses of >60 cm located beside the road (black arrows in Fig. 8), and higher values (>20%) located in specific zones with thicknesses

of <1 m (ellipses in Fig. 8). The location of lower and higher porosity values is conditioned by the spatial location of lower and higher values of input data. The porosity variation in the model is divided into four main intervals, with more or less defined geometries, as enumerated in Table 3. The porosity background of interval 3 (16–19%) is dominant, with intervals 1 (6–11%) and 4 (19%–22%) evolving within it; interval 2 (11–16%) is usually associated with interval 1.

**Table 3: Geometry of porosity patches for a given interval of values.**

Interval Code	Porosity interval (%)	Shape	Length (m)	Width (m)	Thickness (m)
1	6-11	spherical	5-10	5-30	0.2 - 1.4
2	11-16	around patch 1			0.2 - 1.6
3	16-19	Background everywhere			0.2 - 3
4	19-22	more or less elongated patches in X direction	10-20	5-40	0.2 - 3

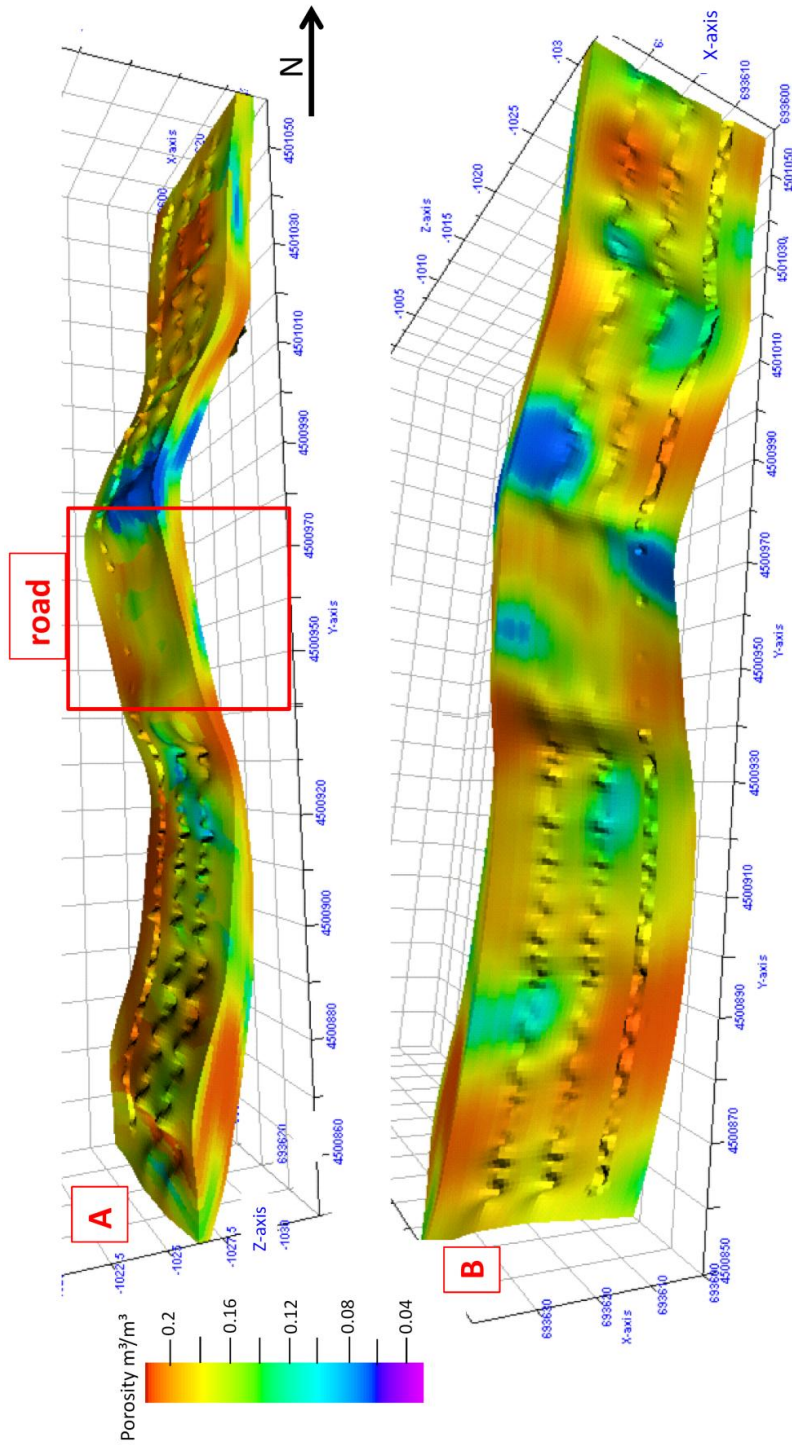
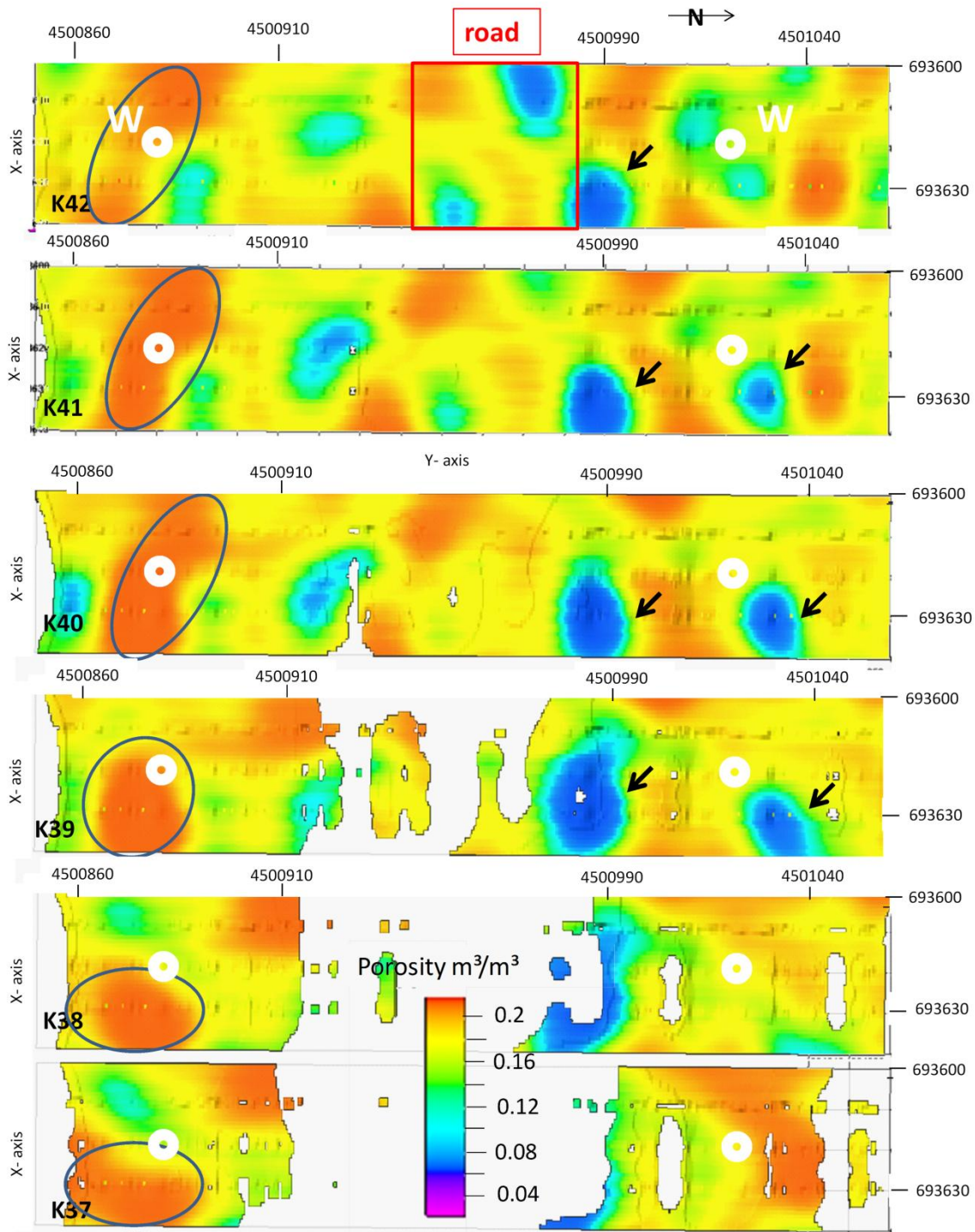


Fig. 7: Tsunami porosity model: (A) perspective from the East, and (B) perspective from the bottom. Vertical scale exaggerated is 4x. The small irregularities in the surface are due to artifacts when generating the maps of the layer boundaries.



**Fig. 8: Layer-by-layer evolution of the porosity model of the Tsunami deposit from the bottom (K42) to the upper (K37) layers. The arrows indicate patches of lower porosity values (< 8%). The ellipses indicate the zones of higher porosity values (>20%). The location of well injector in the simulation cases is the point marked “W”.**

The permeability modelling involved distributing both vertical ( $K_v$ ) and horizontal ( $K_h$ ) permeabilities into the 3D grid. Two main characteristics describe the distribution of measured permeability values in 29 samples: (1) vertical and horizontal permeabilities are strongly correlated (correlation coefficient of 0.85) (Fig. 9), and the permeability behaviour is

assumed to be isotropic; and (2) the strong correlation between porosity and horizontal permeability (Fig. 5). The permeability model was constructed as a function of the porosity model in the X, Y and Z directions, each assuming the same model for  $K_h(x)$ ,  $K_h(y)$  and  $K_v(z)$ . The correlation factor between measured permeability and porosity is 0.82; it is assumed that permeability depends on porosity by a regression function of linear relation (Fig. 5, Equation 1),

$$Y = 0.091EXP(25.713 * x) \tag{Eq. 1}$$

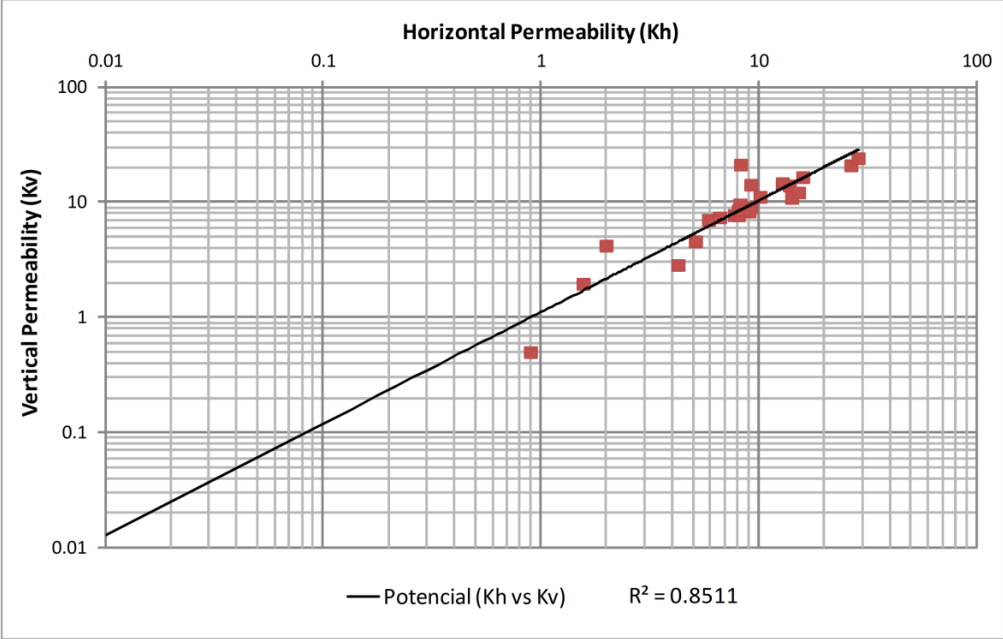


**Fig. 9: Horizontal permeability (Kh) versus vertical permeability (Kv) for all samples (Tsunami and b.i/inlet deposits).**

When applying equation 1 to distribute  $K_h$  values in the tsunami deposit, the measured permeability values were not up-scaled to the 3D grid. The permeability model depends on the porosity model, and the permeability distribution in the model evolves according to the porosity distribution (Fig. 10); however, the permeability values show less variability than the porosity values. Permeability values of  $<1$  mD are found in the North sector of the model, at the upper layers with a thickness of 0.4 m (arrows in Fig. 10).

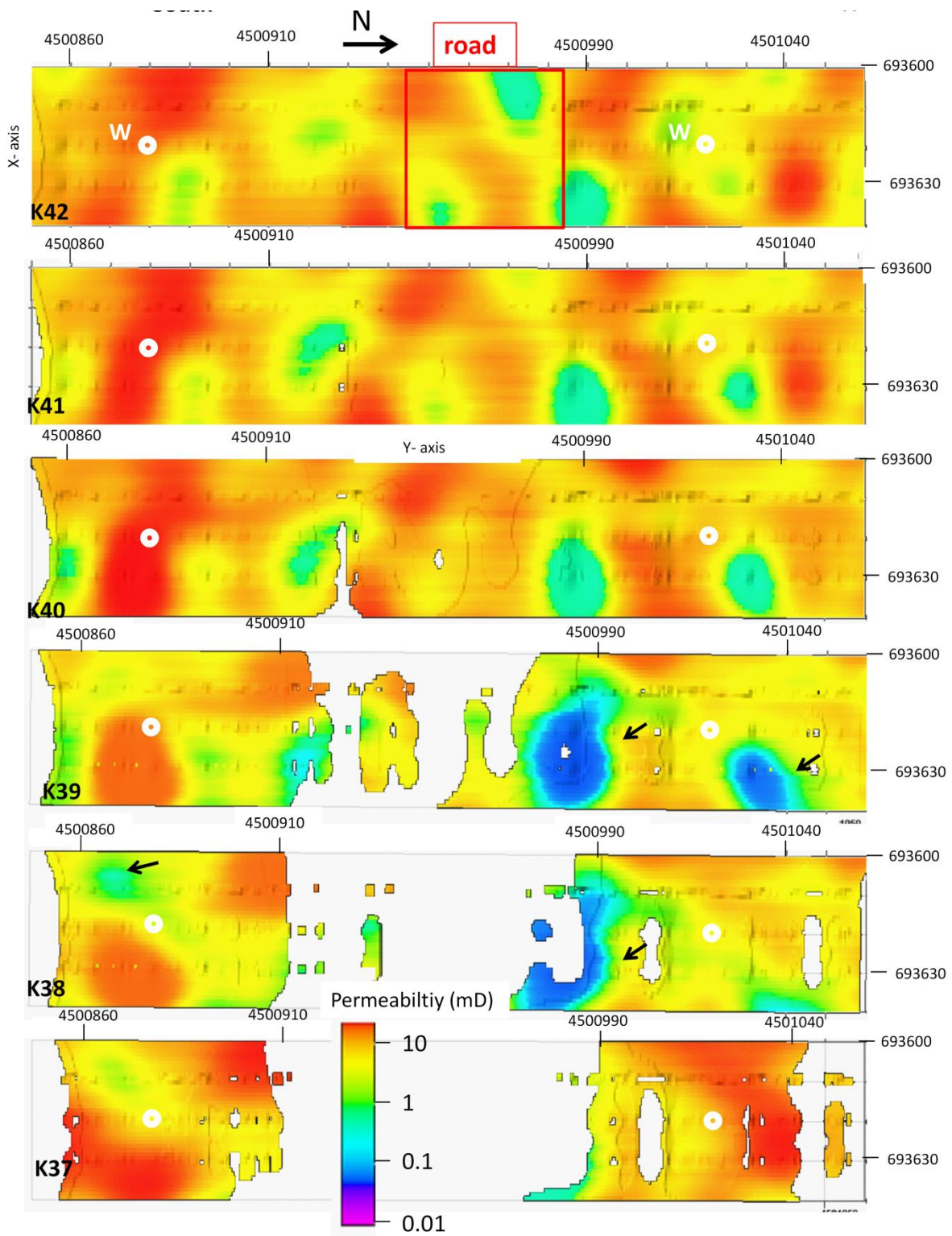


**Fig. 10: Layer-by-layer permeability model for the Tsunami deposit, from the bottom (K42) to the upper (K37) layers. The arrows indicate the zones of lower permeability values (<0.1 mD). The location of well injector in the simulation cases is the point marked 'W'.**

## 2.2. BARRIER-ISLAND – TIDAL INLET RESERVOIR MODEL

Veloso *et al.* (2016) showed the good correlation between the measured porosity and the sorting and cement facies (Fig. 11); facies were classified based on petrophysical characteristics determined from 27 plugs. The porosity distribution was divided into intervals according to sorting and cemented facies (Table 4); lower porosity values were assigned to the CSs facies and higher values to the WSs facies. Clear lithological heterogeneities were observed between outcrop sectors (Fig. 3), the WSs facies is located principally in the South sector and the CSs facies is in the North sector (Table 4). Fig. 12 and Fig. 13 illustrate the porosity and facies models, from the East and West perspectives, respectively. The porosity variations in the MSs and PSs facies are important (Table 4), and create a contrasting of porosity in some zones (see the ellipses in Fig. 12 and 13).

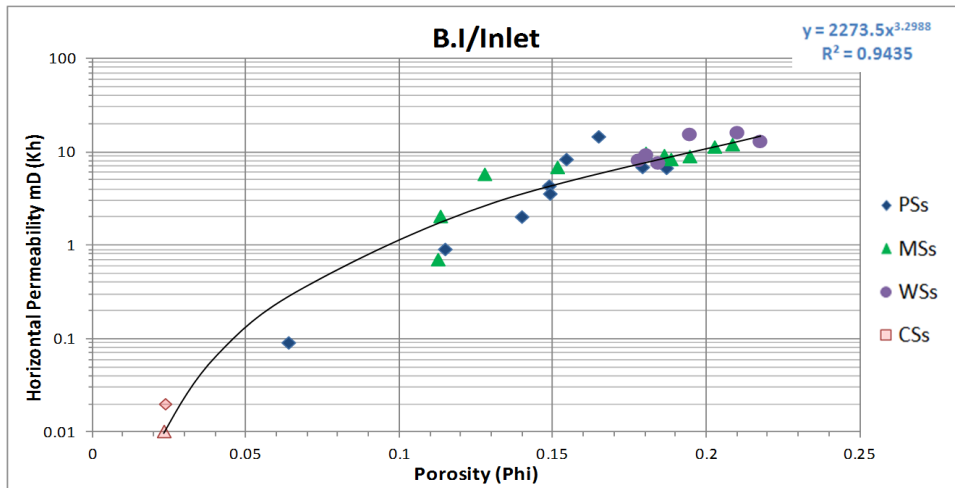


**Fig. 11: Phi versus Kh plot for the b.i./inlet lithofacies, classified by sorting and cemented facies class. The cemented samples (CSs class) are shown by pale red symbols with the point shape representing the sub-classification of sample according to their sand sorting.**

**Table 4: Measured porosity intervals in the b.i./inlet deposit grouped by sorting and cemented facies.**

Sorting Facies class	CSs	PSs	MSs	WSs
Porosity interval (%)	0-6	6-17	11-21	17-22
Facies Fraction in North sector	100%	66%	10%	0%
Facies Fraction in South sector	0%	33%	90%	100%

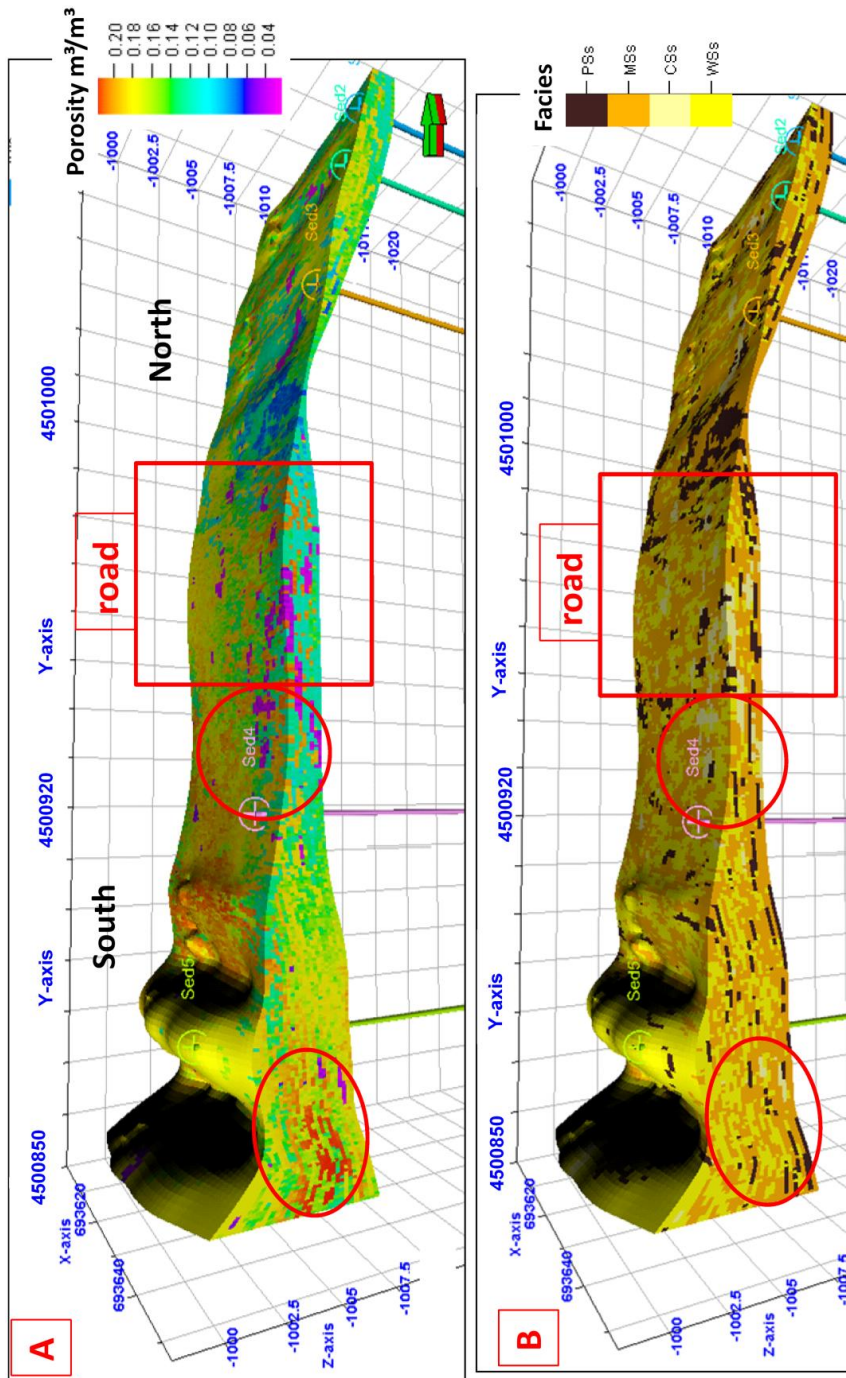


Fig. 12: View from the East of b.i./inlet models. The sedimentary sections are represented as wells. The green/red arrows indicate North, and green shading indicates the top of the model. The vertical exaggeration is 4x. The ellipses indicate the zones of high permeability within a given facies. (A) Porosity model. (B) Facies model.

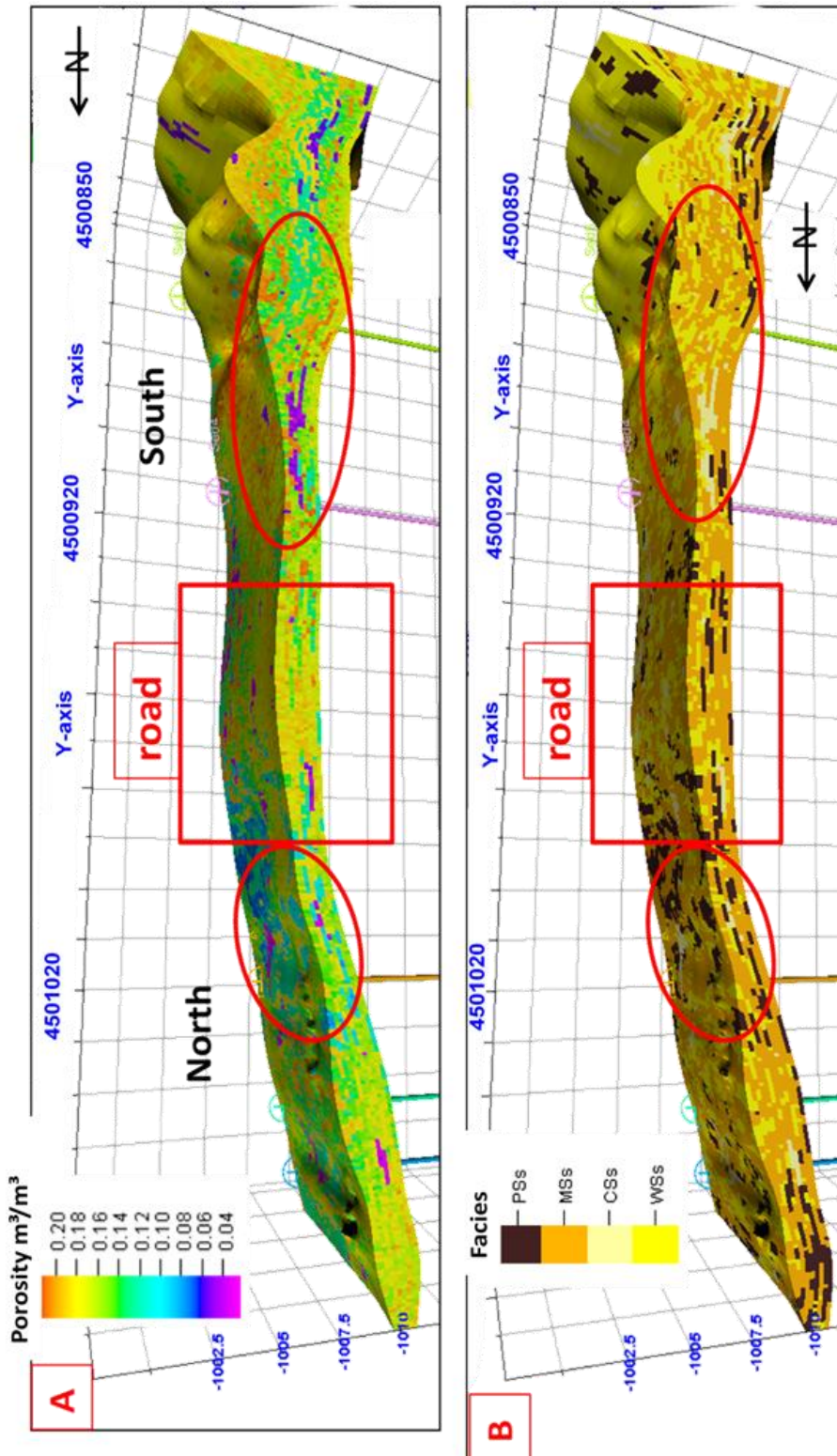


Fig. 13: View from the West of the b.i./inlet models. North is indicated by the green/red arrows; the top of the model is indicated by green shading. The vertical exaggeration is 4x. The ellipses indicate the zone of high permeability contrast within a given facies. (A) b.i./inlet porosity model. (B) B.i./inlet facies model.

The vertical layer-by-layer evolution of porosity (Fig. 14) shows an increase in porosity values towards the upper layers, with higher values in the South sector. The

variation of porosity values evolves in two main directions, as indicated by the large arrows in Fig. 14: (1) a NNW–SSE direction, related to variation in porosity values <16%; and (2) a N–S direction, related to variation in porosity values >16%; the lowest values (<6%), corresponding to CSs facies patches (Fig. 14) and are located mainly in the North sector. The main statistics of modelled and measured porosities are similar (Table 5).

**Table 5: Statistics measured and modelled porosities for the b.i./inlet deposit.**

Porosity (%)	Measured	Modelled
Min:	0.02	0.02
Max:	0.22	0.22
Delta:	0.19	0.19
Number of defined values:	27	199822
Mean:	0.15	0.16
Std. dev.	0.05	0.04
Variance:	0	0
Covariance:	0.33	0.25

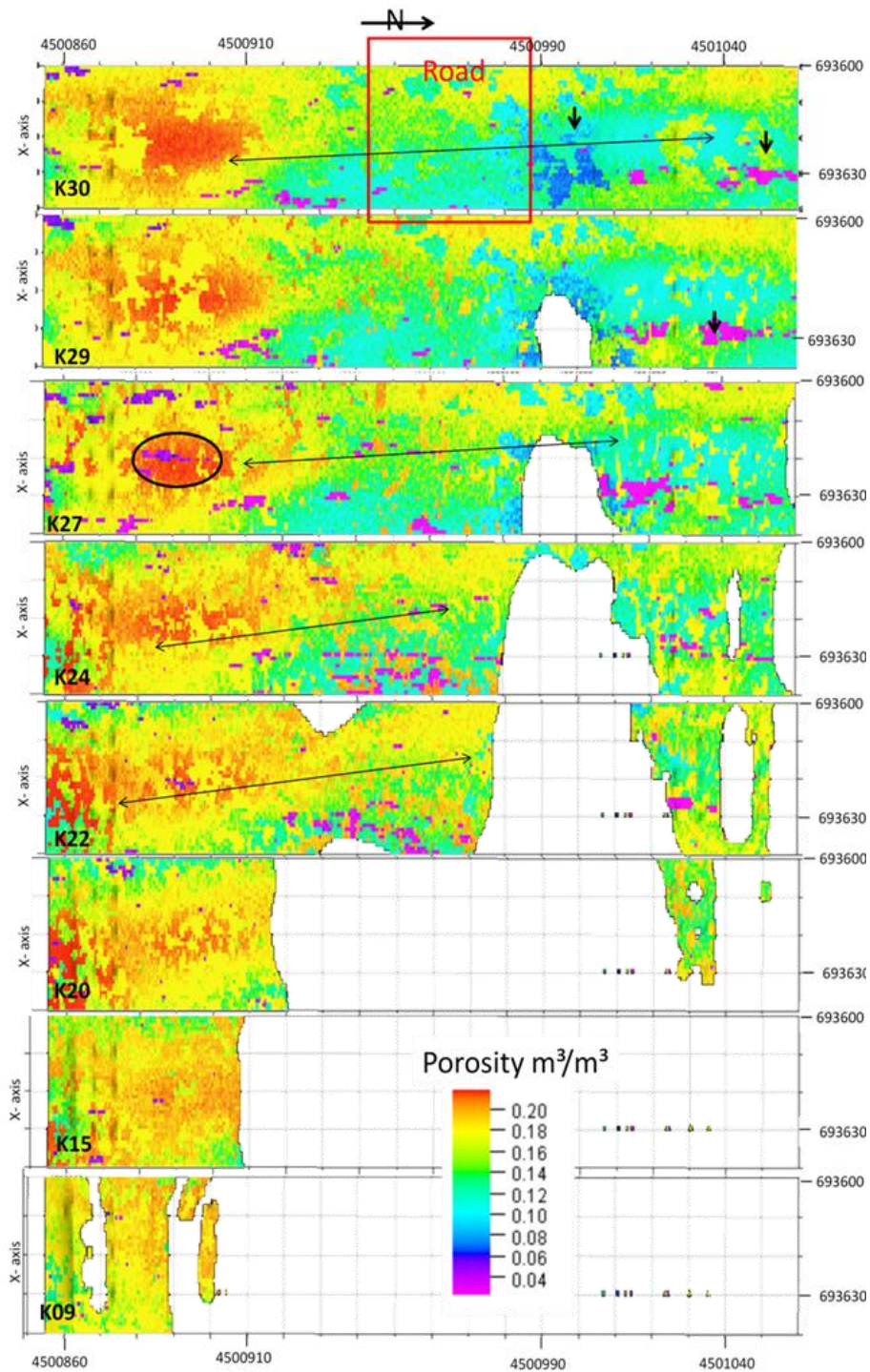


**Fig. 14: Vertical evolution of the b.i./inlet porosity model from the bottom layer (K30) to the upper layers (K15, K09). The large arrows indicate the apparent lateral trend in porosity; the small vertical arrows and the circled zones indicate patches of lower porosity.**

The same methodology used in the modelling of tsunami permeability was applied in the modelling of the b.i./inlet deposit. The 27 permeabilities measured on plugs exhibit two main characteristics: (1) a correlation coefficient of 0.85 between the vertical ( $K_v$ ) and horizontal ( $K_h$ ) permeabilities (Fig. 9), the permeability was assigned as isotropic; and (2) a correlation coefficient of 0.94 between the porosity and the horizontal permeability. Thus,

the permeability model was constructed as a function of the porosity model for X, Y and Z permeability directions, and using the same model for  $K_h(x)$ ,  $K_h(y)$  and  $K_v(z)$ . The dependence of permeability on porosity is described by a power regression function (Equation 2):

$$Y = 2273 * x^{3.3} \quad (\text{Eq. 2})$$

where  $Y$  is the permeability and  $x$  is the porosity (Fig. 11).

Equation 2 was applied to distribute permeability ( $K_h$ ) in b.i./inlet deposit; the measured permeability values were not up-scaled to the 3D grid. The layer-by-layer permeability model is given in Fig. 15, from the bottom layer (K30) to the upper layers (K09, K15, etc.). Because permeability is conditioned by porosity, the heterogeneity in permeability values in the model (Fig. 15) is very similar to that in the porosity model (Fig. 14), with the orientation of trends being similar to those of porosity (large arrows in Fig. 15); however, the variation in the permeability model was smoothed in comparison to those in the porosity model.

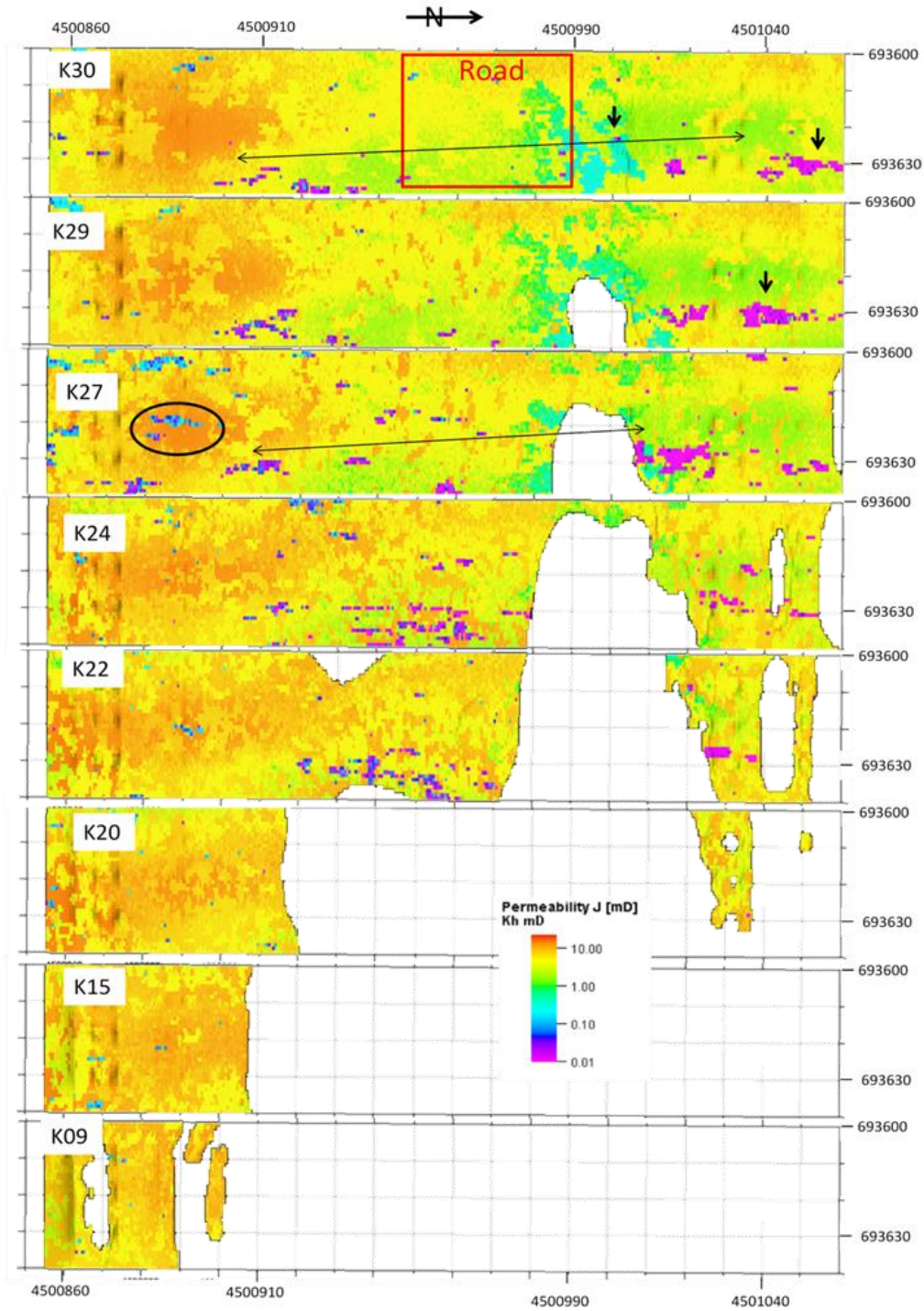


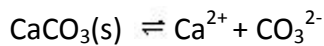
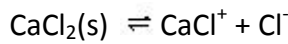
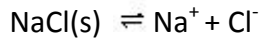
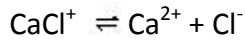
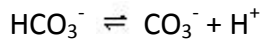
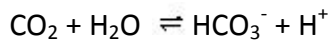
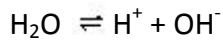
Fig. 15: Vertical evolution of the b.i./inlet permeability model from the bottom layer (K30) to the upper layers (K15, K09). The large arrows indicate the apparent trends of lateral permeability variations; the small arrows and circles indicate regions of lower permeability.

### 3. Fluid Model and its properties

The chemical reactivity of CO<sub>2</sub> as supercritical fluid with brine in reservoirs is an important determinant of its flow behaviour. The partitioning of CO<sub>2</sub> between aqueous and gas phases is strongly dependent on composition of fluid model, temperature and pressure

(IPCC, 2005). The fluid model defines fluid components and phases in the reservoir at the initial conditions. During the simulation, the properties of fluid model components, such as density, viscosity and pH, change according to CO<sub>2</sub> activity within brine. The simulator Eclipse300 (E300), used in this study, is a compositional simulator based on a cubic equation of state and a pressure-dependent permeability value. To model geological conditions in saline storage aquifers, the CO2STORE option of E300 offers the possibility of modelling three phases: a CO<sub>2</sub>-rich phase (labelled 'gas'), an H<sub>2</sub>O-rich phase (labelled liquid) and a solid phase. This option gives accurate mutual solubilities of CO<sub>2</sub> in water, and water in the CO<sub>2</sub>-rich phase. Solids (salts) are included and described as components of the liquid and solid phases. Technical descriptions reported here are found in the Eclipse Technical Descriptions, Version 2013.1 (Schlumberger, 2013a).

The fluid model of both tsunami and b.i./inlet reservoirs has 4 components in two phases, a CO<sub>2</sub>-rich gas phase and a H<sub>2</sub>O-rich liquid phase. The mutual solubility and partitioning of CO<sub>2</sub> and H<sub>2</sub>O in aqueous and gas phases during simulation are calculated to match the experimental data of Spycher and Pruess (2005). The salt components (NaCl and CaCl<sub>2</sub>) can precipitated as solid phase during the simulation; the salt equilibrium in the reservoir is calculated according to reactions (Schlumberger, 2013a) as following:



The dissolved salts are essentially non volatile and formulation hardly changes. In salinity ranging up to ionic strength of around 6 molal (below halite saturation), the water activity equals its mole fraction on the basis of a fully ionized salt. Thus, the water mole fraction in the CO<sub>2</sub>-rich phase ( $y_{\text{H}_2\text{O}}$ , Equation 3) and the CO<sub>2</sub> mole fraction in the aqueous phase ( $x_{\text{CO}_2}$ , Equation 4) are respectively expressed as (Spycher and Pruess, 2005):

$$y_{\text{H}_2\text{O}} = \frac{K_{\text{H}_2\text{O}}^0}{\Phi_{\text{H}_2\text{O}} P_{\text{tot}}} \exp\left(\frac{(P-P^0)\bar{V}_{\text{H}_2\text{O}}}{RT}\right) \quad (\text{Eq.3})$$

$$x_{\text{CO}_2} = \frac{\Phi_{\text{CO}_2} P_{\text{tot}}}{55.508 \gamma_x^i K_{\text{CO}_2(\text{gas})}^0} \exp\left(-\frac{(P-P^0)\bar{V}_{\text{CO}_2}}{RT}\right) \quad (\text{Eq.4})$$

$K^0$  is the thermodynamic equilibrium constant for each component at temperature T and reference pressure

$P^0=1$  bar, for respective reactions  $\text{H}_2\text{O}(\text{liquid}) \rightleftharpoons \text{H}_2\text{O}(\text{gas})$  and  $\text{CO}_2(\text{aqueous}) \rightleftharpoons \text{CO}_2(\text{gas/liquid})$ .  
 $P$  is total pressure.  
 $V$  is the average partial molar volume of each pure condensed phase over the pressure range  $P^0$ - $P$ .  
 $F$  is the fugacity coefficient of component:  $\text{CO}_2$  and  $\text{H}_2\text{O}$  in their respective rich phase.  $\text{CO}_2$  is compressed gas.  
 $R$  is the gas constant.  
 $\gamma'_x$  is the activity coefficient for aqueous  $\text{CO}_2$ .

The amount of  $\text{H}_2\text{O}$  in the  $\text{CO}_2$ -rich phase is small, such that  $\text{CO}_2$  properties can be approximated by those of pure  $\text{CO}_2$  (Spycher *et al.*, 2003).

The temperature of fluid model was constant of  $32^\circ\text{C}$  and the initial equilibrium pressure was 103 bars for Tsunami model and 98 bars for b.i./inlet model, which correspond to the hydrostatic pressure at a burial depth of 1003 and 998, respectively. At this range of temperature ( $T$ ) and pressure ( $P$ ), the state of  $\text{CO}_2$  is very close to its critical point in  $P \times T$  phase diagram of pure  $\text{CO}_2$  (Fig. 16); the  $\text{CO}_2$  in a supercritical state behaves as a dense phase gas (Fig. 16, IPCC, 2005).

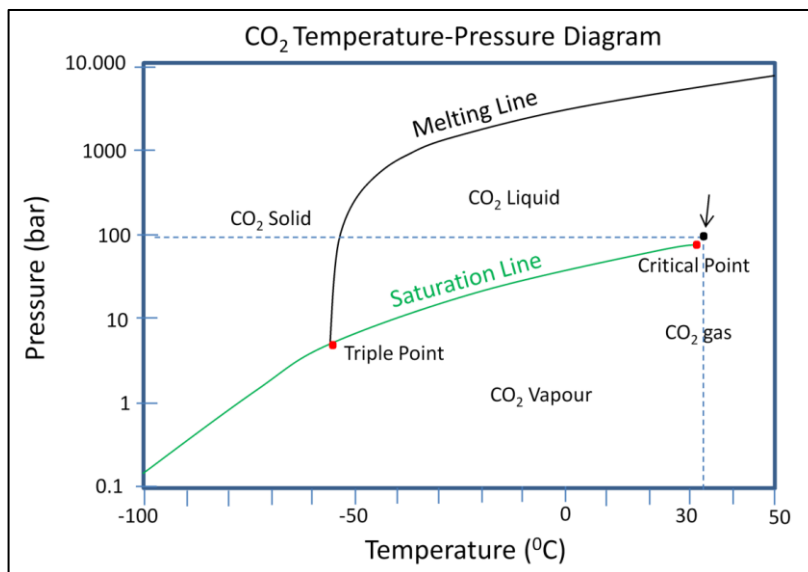


**Fig. 16: Pressure–temperature phase diagram of pure  $\text{CO}_2$ . The arrow indicates the average initial pressure and temperature conditions of the two reservoirs examined in this study. Modified from IPCC, 2005 (from ChemicalLogic Corporation, 1999).**

### 3.1. DENSITY

The density of supercritical  $\text{CO}_2$  (at depths below 800 m, Fig. 16) range from 50 to 80% of the density of water, under these conditions, buoyancy forces tend to drive  $\text{CO}_2$  upwards (IPCC, 2005). However, at the interface between supercritical  $\text{CO}_2$  and brine,  $\text{CO}_2$  dissolves in the brine to form a solution that is heavier than the underlying brine (Nomeli *et al.*, 2014). The brine saturated with  $\text{CO}_2$  will ultimately sink to the bottom of the reservoir, while non-saturated water will rise and can dissolve more  $\text{CO}_2$ . This process however is

rather slow and the dissolution depends on the contact between the brine and the carbon dioxide phase (Green *et al.*, 2009; Vogel, 2009).

The simulator (E300) leads to fast density changing for the CO<sub>2</sub> rich-gas phase and H<sub>2</sub>O rich phase, the water density is influenced by the dissolution of CO<sub>2</sub> in the brine. The gas density is calculated by a cubic equation of state (EOS), modified from Redlich-Kwong EOS and adjusted to match experimental results of Spycher and Pruess (2005). For the H<sub>2</sub>O rich phase, density is firstly computed from the density of pure water following the thermodynamical properties detailed in “The International Association for the Properties of Water and Steam” (IAPWS-IF97), then the Ezrokhi’s method (Equations 5 and 6) is applied to calculate the effect of salt and CO<sub>2</sub> (Prost, 2008; e.g. Zaytsev and Aseyev, 1993).

$$\lg \rho = \lg \rho_0 + \sum (A_i c_i) \quad (\text{Eq. 5})$$

$\rho$  is the density of water and  $\rho_0$  is the density of pure water.

$c_i$  is the mass fraction of each component.

$A_i$  is the activity coefficient for each component

$$A_i = b_{0,i} + b_{1,i}T + b_{2,i}T^2 \quad (\text{Eq. 6})$$

$b_n$ ,  $i$  are coefficients for a series of electrolytes and

$T$  stands for temperature in degree Celsius.

Solid density of NaCl and CaCl<sub>2</sub> were respectively 2170 kg/m<sup>3</sup> and 2150 kg/m<sup>3</sup> at the reference pressure of 100 bars and temperature of 32°C (Schlumberger, 2013a).

### 3.2. VISCOSITY

Supercritical CO<sub>2</sub> is much less viscous than water (by an order of magnitude or more) and migration is controlled by the contrast in mobility of CO<sub>2</sub> and the in situ formation fluids (IPCC, 2005; Celia *et al.*, 2005; Nordbotten *et al.*, 2005). The viscosity of CO<sub>2</sub> is calculated from the equations of Vesovic *et al.* (1990) and Fenghour *et al.* (1998) which declare the viscosity as a function of temperature and pressure. The viscosity of H<sub>2</sub>O rich phase is calculated as the method of calculation of H<sub>2</sub>O density. Firstly, the H<sub>2</sub>O viscosity is calculated for pure water and then the Ezrokhi’s method is applied (Equations 5 and 6).

### 3.3. pH CALCULATION

The dissociation of CO<sub>2</sub> leads to the transformation of dissolved CO<sub>2</sub> into bicarbonate ions (ionic trapping) inducing a lowering of the pH in the formation water (Chadwick *et al.*, 2008). The pH is calculated as given in the equation 7 (Schlumberger, 2013a):

$$pH = -\log (A_H m_H) \quad (\text{Eq.7})$$

$A_H$  is the activity coefficient of the H<sup>+</sup> ion.

$m_H$  is the molality of the H<sup>+</sup> ion.

### 3.4. SATURATION FUNCTIONS

Interactions between the CO<sub>2</sub> and H<sub>2</sub>O rich-phases are represented at the grid-block scale by the capillary pressure and relative permeability functions (Doughty, 2007), which

depend on the fluid saturation in the porous media (Corey, 1954) or in the grid block. Many studies have showed the impact and the sensibility of the capillary pressure and relative permeability on the mechanism of CO<sub>2</sub> storage, such as the residual trapping and the CO<sub>2</sub> dissolution in the brine phase (Juanes et al. 2006; Spiteri and Juanes, 2006; Plug and Bruining, 2007; Pini et al., 2012; Boxiao et al., 2013; Frykman et al., 2013). The water (WSF) and gas saturation (GSF) functions of Table 6 were taken from the CO2STORE.data Schlumberger study case (Schlumberger, 2013a), as well as the gas-water drainage capillary pressure (Pcog). However, sensibility tests of these parameters for the Camarillas Fm. are strongly recommended, because the capillary heterogeneity in the reservoir induces the capillary trapping and reduces the migration of CO<sub>2</sub> plume (Frykman *et al.*, 2013).

**Table 6: Water (WSF) and Gas (GSF) saturation function used in this study. Table headings: Sw: water saturation; Krw: relative water permeability at a given saturation; Sg: gas saturation; Krg: relative gas permeability at a given saturation; DrainPcog: gas-water drainage capillarity pressure.**

WSF (water saturation function)		GSF (Gas saturation function)		
Sw	Krw	Sg	Krg	Drain Pcog (bars)
0.3	0	0	0	0
0.38	0.000152	0.08	0	0.6
0.46	0.002439	0.16	0.000407	0.78
0.53	0.012346	0.23	0.005831	0.93
0.61	0.039018	0.31	0.024131	1.09
0.69	0.09526	0.39	0.064892	1.26
0.77	0.197531	0.47	0.140566	1.49
0.84	0.36595	0.54	0.269314	1.84
0.92	0.624295	0.62	0.484797	2.53
1	1	0.7	1	10

### 3.5. DIFFUSION

Diffusion or mass transfer is the dominant mechanism to transport dissolved CO<sub>2</sub> into the low-permeability regions from the high-permeability pathways (Chang *et al.*, 2014). The molecular diffusion in E300 is calculated for diffusive flows in terms of the liquid mole fractions and vapour mole fractions. The diffusion coefficients ( $D_i$ ) of each component, entered by user, solve the condition (equation 8) of Reid *et al.* (1987) to define the molar vapour flux ( $J_i$ ) of each component per unit of area:

$$J_i = -cD_i \frac{\partial x_i}{\partial a} \quad (\text{Eq.8})$$

$c$  is the molar concentration

$\frac{\partial x_i}{\partial a}$  is the molar concentration gradient of component  $i$

Water diffusion coefficients are typically an order of magnitude lower than gas diffusion coefficients (Schlumberger, 2013a) and were entered for the four components of the fluid model. Although the diffusion mechanism is slow and not relevant to time scale of this study, Schlumberger recommended (Schlumberger, 2013a) the utilization of diffusion coefficients, which are summarized in Table 7.

**Table 7: Diffusion coefficients used in this study**

Water diffusion coefficients				Gas diffusion coefficients	
H <sub>2</sub> O	CO <sub>2</sub>	NaCl	CaCl <sub>2</sub>	H <sub>2</sub> O	CO <sub>2</sub>
0.0001	0.0001	0.0001	0.0001	0.001	0.001

## 4. Results of reservoir simulation

### 4.1. Model boundary conditions and model initialization

Before proceeding with the simulation, the pore volume of the four end faces of each reservoir model was multiplied by 1000 (Fig. 17) to avoid a fast pressure build-up related to the small size of reservoir models and low volume of the reservoir (rm<sup>3</sup>). The grid blocks of end faces represents ~5% of the total grid blocks with defined continuous values for both reservoir models (Table 8). Their total pore volume correspond to ~98% of the total pore volume in the reservoir, however the amount of CO<sub>2</sub> activity (in aqueous phase) and the molar density of the CO<sub>2</sub> per reservoir volume into these grid blocks, at the end of simulation, represented less than 1% of the total CO<sub>2</sub> in the entire model (Table 8) for both reservoirs. The flow is inactive outside the reservoirs.

**Table 8: Summary of defined values for pore volume and CO<sub>2</sub> activity in the entire model (column ALL), boundary zone of pore volume multiplied by 1000 (MULTPV) and the main zone with the original pore volume (MUTPVNO).**

Statistics for pore volume (rm <sup>3</sup> ) at initial conditions			
	ALL	MULTPV	MUTPVNO
<b>InletV3</b>			
Type of data:	Continuous		
Number of defined values (active cells):	199818	10110	189708
Sum of values:	175551	172080	3471
volume percentage:	100	98.02	1.97
<b>TsunV5</b>			
Type of data:	Continuous		
Number of defined values (active cells):	92659	4868	87791
Sum of values:	96108.69	94186.52	1922.17
volume percentage:	100	98	2
Statistics for aCO <sub>2</sub> (CO <sub>2</sub> Activity) at end of simulation			
	ALL	MULTPV	MUTPVNO
<b>InletV3</b>			

<b>Number of defined values (active cells):</b>	199818	10110	189708
<b>Sum of values:</b>	12565.493	108.3761	12446.9
<b>volume percentage:</b>	100	0.86248984	99.0561
<b>TsunV5</b>			
<b>Number of defined values (active cells):</b>	92659	4868	87791
<b>Sum of values:</b>	10417.1272	79.5426	10341.9
<b>volume percentage:</b>	100	0.7635752	99.278
<b>Statistics for CO<sub>2</sub> moles per reservoir volume at end of simulation (kg-mole/rm<sup>3</sup>)</b>			
	<b>ALL</b>	<b>MULTPV</b>	<b>MULTPVNO</b>
<b>InletV5</b>			
<b>Number of defined values (active cells):</b>	199818	10110	189708
<b>Sum of values:</b>	221779.95	32.27	221530.6
<b>volume percentage:</b>	100	0.1	99.9
<b>TsunV2</b>			
<b>Number of defined values (active cells):</b>	92659	4868	87791
<b>Sum of values:</b>	152621.84	6.18	152615.66
<b>volume percentage:</b>	100	0.01	99.99

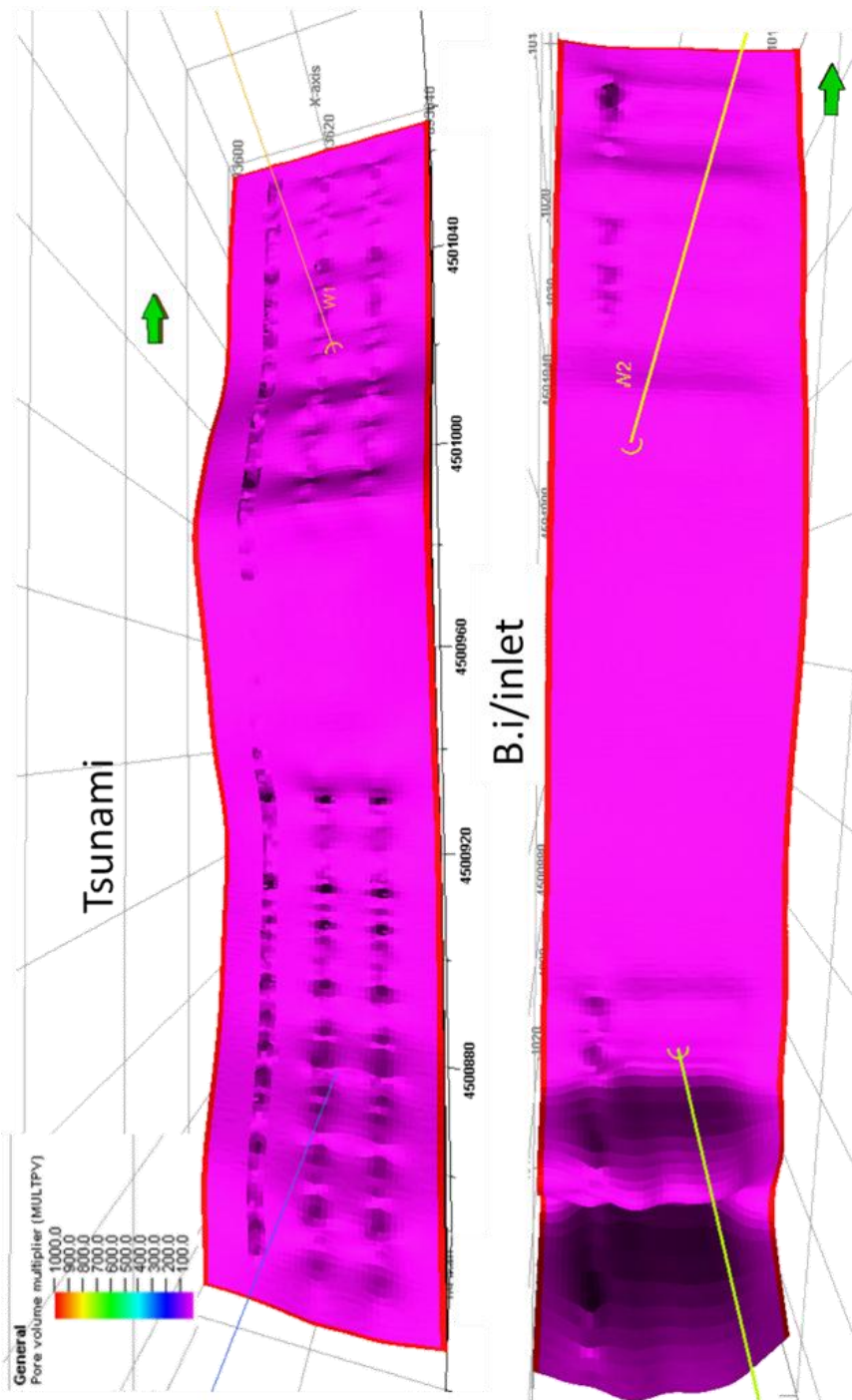


Fig. 17: Top view of tsunami and b.i./inlet reservoir model showing the four end faces of each reservoir model which were multiplied by 1000. Vertical scale is exaggerated of 4x

The simulation of CO<sub>2</sub> injection was performed independently for each reservoir model. The initial conditions and the properties of fluid model were identical in both reservoirs and are listed in Table 9. The components of fluid model at the initial conditions were H<sub>2</sub>O, NaCl and CaCl<sub>2</sub> in aqueous phase. The CO<sub>2</sub> was injected as a dry gas.

Table 9: Initial conditions of simulation studies

Initial Conditions	
H <sub>2</sub> O mole fraction	0.9109

CO <sub>2</sub> mole fraction	0			
NaCl mole fraction	0.0741			
CaCl <sub>2</sub> mole fraction	0.015			
Temperature	32°C			
	<b>Tsunami case studies</b>		<b>B.i./inlet case studies</b>	
<b>Total pore volume at P(ref): rm<sup>3</sup></b>	96108.7		175551	
<b>Average permeability: mD</b>	10.41		6.85	
<b>Average porosity: m<sup>3</sup>/m<sup>3</sup></b>	0.17		0.16	
<b>Average cell thickness: m</b>	0.21		0.21	
<b>Average pressure: Bar</b>	102.93		98.98	
	Maximum	Minimum	Maximum	Minimum
<b>Depth: m</b>	1031.858	1025.269	1010.96	999.375
<b>Porosity: m<sup>3</sup>/m<sup>3</sup></b>	0.21	0.07	0.22	0.02
<b>Pore Volume:</b>	40.95	0.0017	37.75	0.0005
<b>Permeability X, Y and Z</b>	21.81	0.5	14.89	0.01

Four study cases were run for each reservoir model. The equilibrium pressure at initial conditions corresponds to the burial deep of the top of reservoir, 103 and 99 bars in the tsunami and the b.i./inlet models, respectively. The study cases test the sensibility of the location of injector well and the flow rate on the behaviour of CO<sub>2</sub> in the zone close of the injector well.

#### 4.2. SIMULATION ON THE TSUNAMI RESERVOIR

The Table 10 summarizes the study cases of the tsunami reservoir model in terms of the injection rate, injection time and observation time after injection. The study cases TsunV2 and TsunV3 had the injector well located in the North sector of model, while in the study cases TsunV4 and TsunV5, the injector well was located in the South sector (Fig. 3). The cases TsunV2 and TsunV5 had an injection rate of constant flow of 80 sm<sup>3</sup>/day and the cases TsunV3 and TsunV4 had three different flow rates with each one spaced from another by ~ 1 year of observation time or stopped injection time. In all study cases, the injector well was completed in the 'Y' horizontal direction, connecting 7 grid blocks at the bottom of model. The well diameter at the connection of grid block is 19 cm; this value was required to calculate the connection transmissibility factor and well productivity/injectivity index.

**Table 10: Injection rate, simulation time and observation time after injection of Tsunami study cases**

Case	Flow Rate (sm <sup>3</sup> /day)	Injection time (years)	Observation time (Years)
TsunV2 & TsunV5	80	3.56	3.97
TsunV3 & TsunV4	200	0.92	0.97
	150	0.51	0.97

	100	0.34	3.17
--	-----	------	------

The CO<sub>2</sub> is present in the reservoir as dissolved in the brine (saline water), residual and mobile as gas phase. Table 11 summarizes the CO<sub>2</sub> amount in the reservoir for different CO<sub>2</sub> phases. Although the total amount of CO<sub>2</sub> injected in the cases of different flow rate was 3.7% higher than the cases of constant flow rate, the constant flow rate cases, TsunV2 (northern injector well) and TsunV5 (southern injector well), dissolved quite more CO<sub>2</sub> than the cases TsunV3 and TsunV4 for the respective sector of model. This difference in the amount of injected CO<sub>2</sub> produces a slightly larger plume extension of gas saturation (CO<sub>2</sub>) in the cases of different flow rates (see arrows in Fig. 18B-D and Fig. 19A-C). The maximum saturation of CO<sub>2</sub> gas into the gas plume at the end of simulation reached up 30% and 25% in the cases with the injector well located in the North and South sectors, respectively, independent on the rate regime (Fig. 18 and Fig. 19). During the simulation, the gas saturation in the gas plume up to 45% in the cases of constant flow rate and to 50% in the cases of different flow rates. The average reservoir pressure of all study cases remained ~122 bars at the end of simulation, and up to 130 bars at the bottom hole (BHP) during injection.

**Table 11: Summary of CO<sub>2</sub> distribution into tsunami reservoir at the end of simulation**

	North				South			
	TsunV2 (constant)		TsunV3		TsunV4		TsunV5 (constant)	
<b>Reservoir volume of CO<sub>2</sub> gas (rm<sup>3</sup>)</b>	144.82		151.76		147.34		141.74	
<b>Total injected CO<sub>2</sub> (sm<sup>3</sup>)</b>	103929	100%	107862	100%	107862	100%	103929	100%
<b>Total CO<sub>2</sub> dissolved (kg-mole)</b>	1854.1		1908.3		1986.8		1917.3	
<b>Total CO<sub>2</sub> dissolved: (sm<sup>3</sup>)</b>	43924.7	42.3%	45209.1	41.9%	47068.4	43.6%	45422.6	43.7%
<b>Total CO<sub>2</sub> mobile (kg-mole)</b>	1592.2		1674.5		1551.0		1473.1	
<b>Total CO<sub>2</sub> mobile (sm<sup>3</sup>)</b>	37719.2	36.3%	39669.4	36.8%	36743.5	34.1%	34898.0	33.6%
<b>Total CO<sub>2</sub> residual (kg-mole)</b>	940.7		975.4		1020.4		996.5	
<b>Total CO<sub>2</sub> residual (sm<sup>3</sup>)</b>	22284.9	21.4%	23108.1	21.4%	24174.5	22.4%	23607.8	22.7%
<b>Average Field Pressure (bar)</b>	121.77		122.53		122.38		121.66	

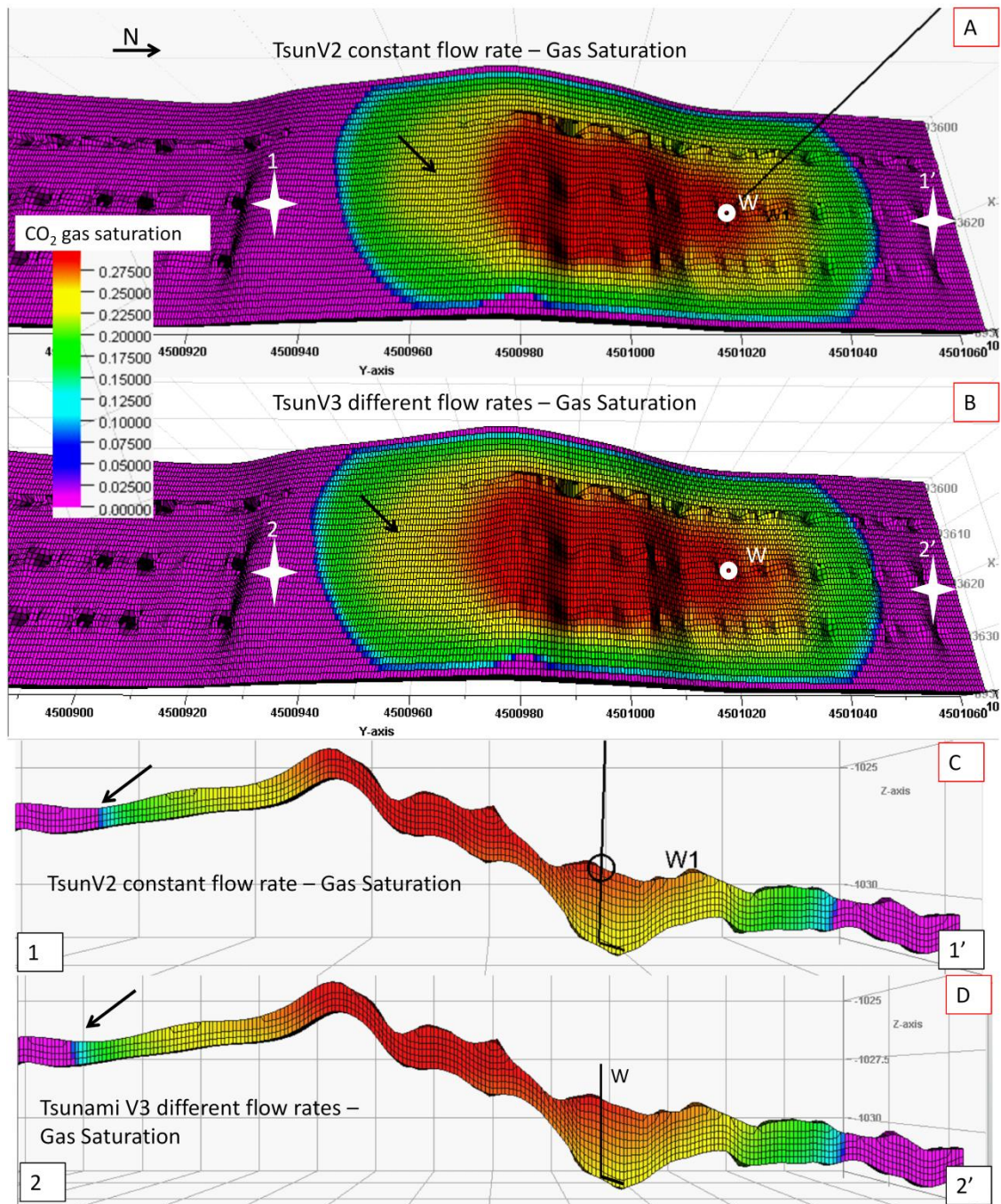


**Fig. 18:** Plume extension of the CO<sub>2</sub> saturation at the end of simulation for Tsunami study cases with the injector well ('W') located in the North sector. Vertical exaggeration of 4x. (A) Reservoir top view of the case TsunV2 with constant flow rate. (B) Reservoir top view of the case TsunV3 with different flow rates. In (A) and (B), the injector well is represented by the point "W" and the arrows indicate the CO<sub>2</sub> saturation of around 24%. (C) North-South cross section of CO<sub>2</sub> saturation between points 1 and 1' in (A) of TsunV2 case; the injector well is represented by vertical bars marked 'W'. (D) North-South cross section of CO<sub>2</sub> saturation between points 2 and 2' in (B). In (C) and (D), the arrows indicate the northern border of the plume extension.

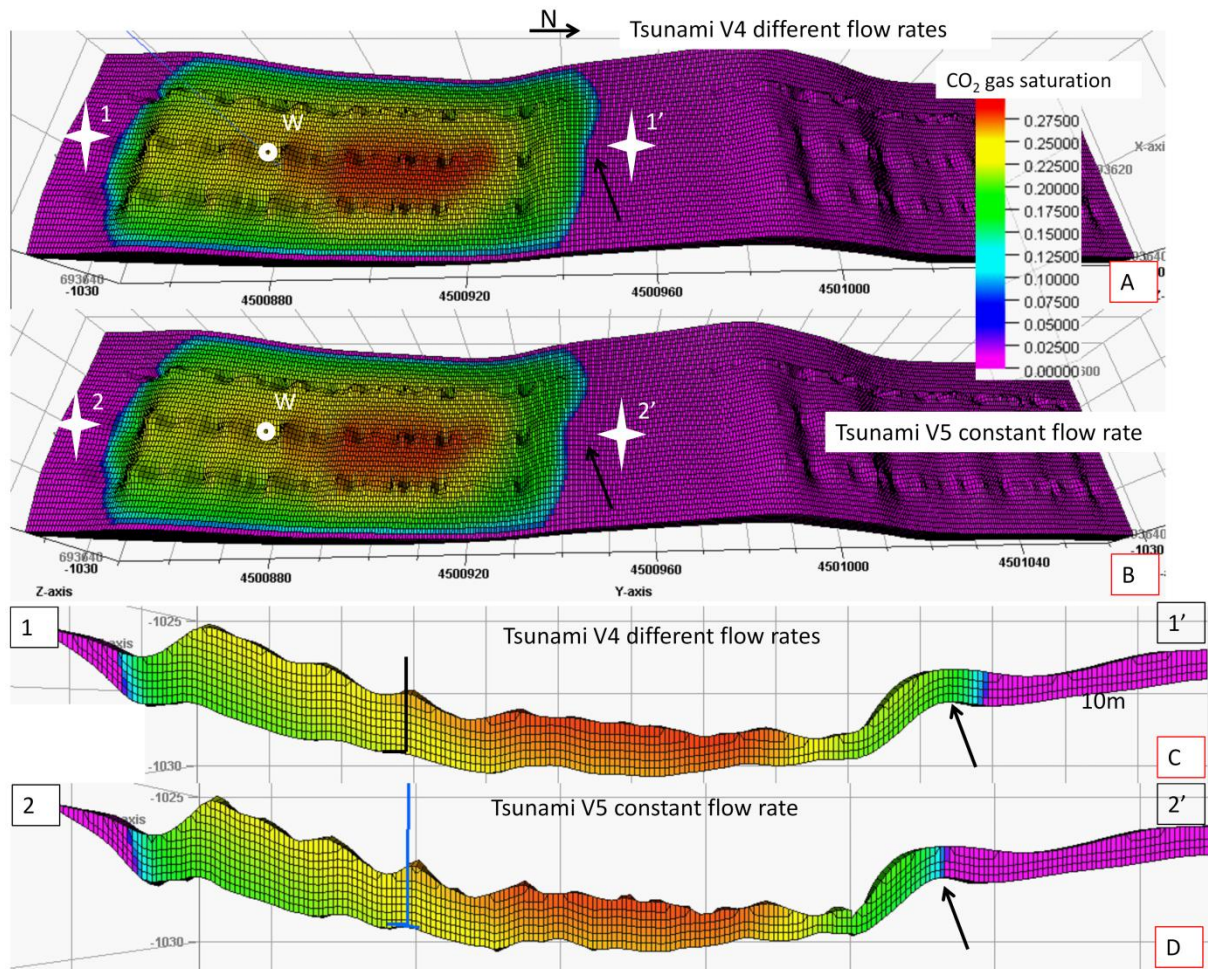


**Fig. 19: Plume extension of CO<sub>2</sub> saturation at the end of simulation for Tsunami study cases with the injector well ('W') in the South sector; arrows indicate the CO<sub>2</sub> plume extension in the North direction. Vertical scale exaggerated of 4x. (A) Reservoir top view of case TsunV4 with different flow rates. (B) Reservoir top view of case TsunV5 with constant flow rate. In (A) and (B), the injector well is represented by the point "W". (C) North-South cross section of CO<sub>2</sub> saturation between points 1 and 1' in (A) at well location. (D) North-South cross section of CO<sub>2</sub> saturation between points 2 and 2' in (B) at well location. The injector well is represented by the vertical bar in (C) and (D).**

#### 4.3. SIMULATION ON THE BARRIER ISLAND – TIDAL INLET DEPOSIT RESERVOIR

Table 12 summarizes the barrier island – tidal inlet (b.i./inlet) study cases in terms of the injection rate, injection time and observation time after injection. The injector well was located in the North sector in the study cases InletV3 and InletV4 and in the South sectors in cases InletV5 and InletV6. The cases InletV4 and InletV5 had a constant flow rate of 260 sm<sup>3</sup>/day and the cases InletV3 and InletV6 had three different flow rates, spaced of ~1.6 year observation time after injection period. In all cases, the injector well was completed in the 'Y' horizontal direction connecting 7 grid blocks at the bottom of model. The well diameter at grid block connection is 19 cm; this value was required to calculate the connection transmissibility factor and the well productivity/injectivity index.

**Table 12: Injection rate, simulation time and observation time after injection of b.i./inlet study cases**

	Injection rate (sm <sup>3</sup> / day)	injection time (year)	Observation time (year)
IV3 and IV6	400	0.54	1.96
	150	0.34	1.45
	150	0.34	1.95
IV4 and IV5	260	1.22	5.34

Table 13 summarizes the amount of CO<sub>2</sub> dissolved in the water, mobile and residual in gas phase for all study cases: The cases with the injector well located in the North (Fig. 20) showed a larger extent of the CO<sub>2</sub> gas plume and a more homogeneous distribution of the CO<sub>2</sub> saturation into the plume in the case of constant flow rate (InletV4) at the end of simulation. The cases InletV5 and InletV6 (southern injector well) showed a similar CO<sub>2</sub> plume extension (Fig. 21), although more ~3% of CO<sub>2</sub> is dissolved in the case of constant flow rate (InletV5) (Table 13). The cases with the injector well in the North sector dissolved more 20% CO<sub>2</sub> than the cases of InletV5 and InletV6. The average reservoir pressure at the end of simulation is similar between study cases (Table 13); maximum BHP during injection was around 130 bars ( $\pm$  3 bars) for study cases of different flow rates (InletV3 and InletV6) and 128 bars and 118 bars for InletV4 (North) and InletV5 (South), respectively.

**Table 13: Summary of CO<sub>2</sub> distribution into b.i./ inlet reservoir at the end of simulation**

	North				South			
	InletV3		InletV4 (constant)		InletV5 (constant)		InletV6	
Reservoir volume of CO <sub>2</sub> gas (rm <sup>3</sup> )	165.13		163.02		232.33		240.38	
Total injected CO <sub>2</sub> (sm <sup>3</sup> )	116240.0	100%	115986.0	100%	115986.0	100%	116240.0	100%
Total CO <sub>2</sub> dissolved (kg-mole)	2102.2		2128.3		937.3		808.1	
Total CO <sub>2</sub> dissolved: (sm <sup>3</sup> )	49801.8	42.8%	50420.5	43.5%	22205.6	19.1%	19144.3	16.5%
Total CO <sub>2</sub> mobile (kg-mole)	1844.7		1726.2		2262.3		2489.0	
Total CO <sub>2</sub> mobile (sm <sup>3</sup> )	43700.4	37.6%	40895.3	35.3%	53594.7	46.2%	58965.2	50.7%
Total CO <sub>2</sub> residual (kg-mole)	959.8		1041.4		1696.3		1609.5	
Total CO <sub>2</sub> residual (sm <sup>3</sup> )	22737.9	19.6%	24670.0	21.3%	40185.0	34.6%	38130.5	32.8%
Average Field Pressure (bar)	111.1		111.0		112.4		112.6	

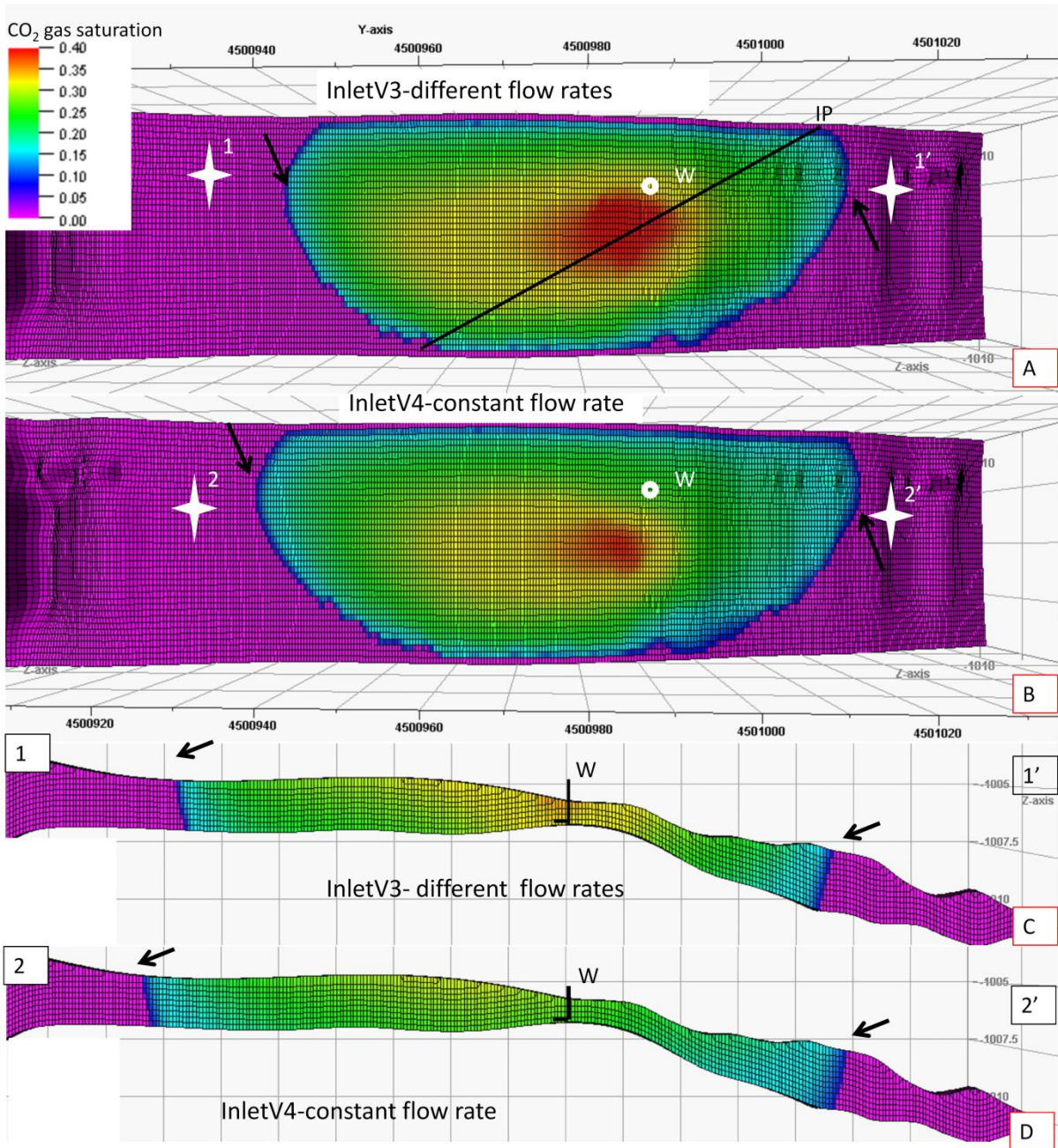


Fig. 20: Plume extension of the CO<sub>2</sub> saturation at the end of simulation for b.i./inlet study cases with the injector well ('W') in the North sector. The arrows indicate the CO<sub>2</sub> plume extension in the North and the South directions. Vertical scale is exaggerated of 4x. View of the reservoir top: (A) the case InletV3 with different flow rates (the line 'IP' is location of the intersection plan in Fig. 24C) and (B) the case InletV4 with constant flow rate. In (A) and (B), the injector well is represented by the point 'W' (C) S-N Cross section of CO<sub>2</sub> saturation between points 1 and 1' in (A). (D) Cross section of CO<sub>2</sub> saturation between points 2 and 2' in (B). The injector well is represented by the vertical bar marked "W" in (C) and (D).

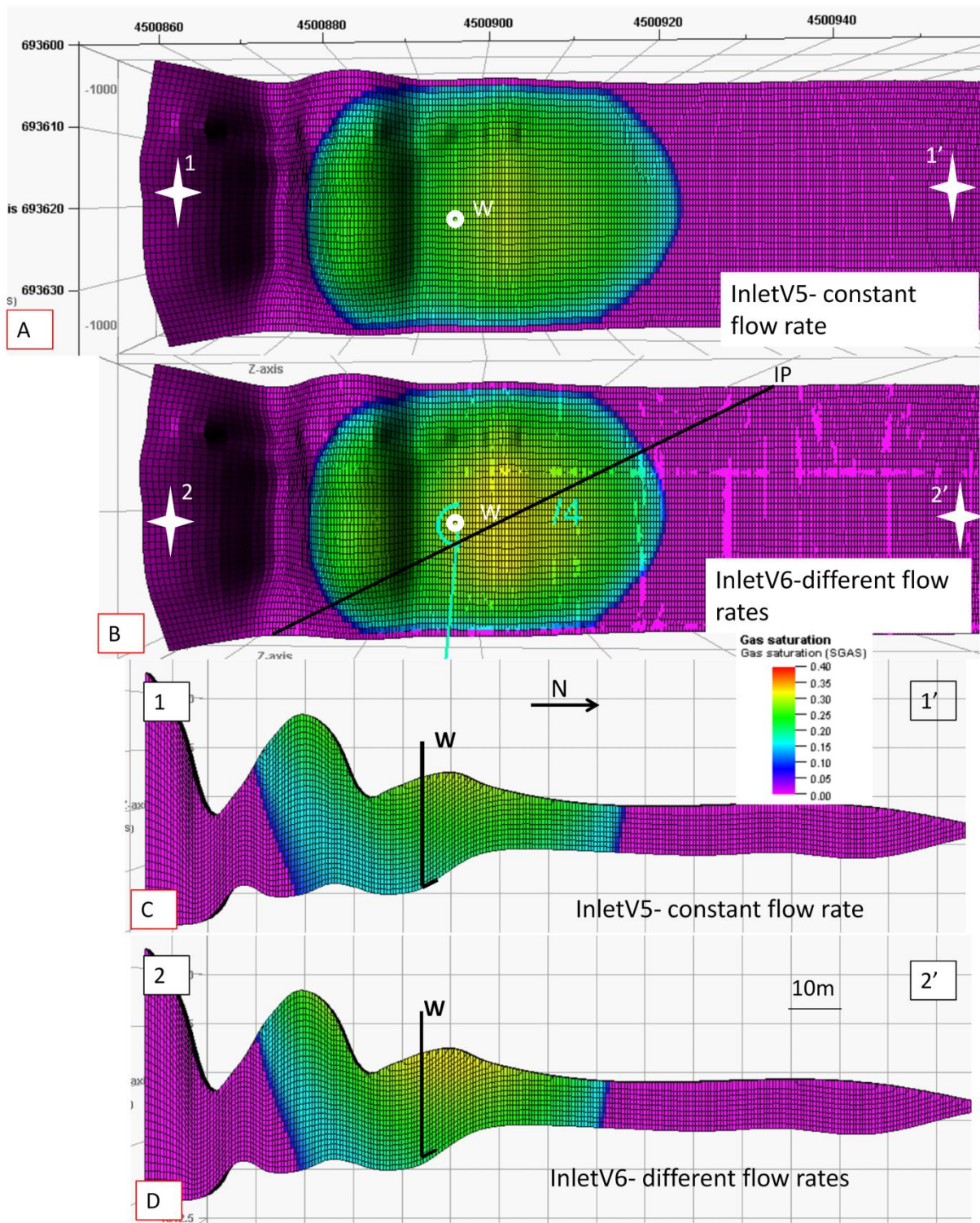


Fig. 21: Plume extension of the CO<sub>2</sub> saturation at the end of simulation for b.i./inlet study cases with the injector well in the South sector ('W'). Vertical scale is exaggerated of 4x. View of the reservoir top: (A) the case InletV5 with constant flow rate and (B) the case InletV6 with different flow rates; the line 'IP' is location of the intersection plan in Fig. 25C. In (A) and (B), the injector well is represented by the point "W". (C) Cross section of the CO<sub>2</sub> saturation between points 1 and 1' in (A). (D) Cross section of CO<sub>2</sub> saturation between points 2 and 2' in (B).

## 5. Discussion

In both reservoir models, around 50-60% of the injected CO<sub>2</sub> was stored in the reservoir as residual gas and as dissolved in the brine at the end of simulation. The short time scale of simulation and the low flow rate of injection allowed observing the CO<sub>2</sub> behaviour in the zone close to injector well without the influence of the boundary conditions. Although the pore volume of boundary grid block represented 98% of total pore volume, these grid blocks represented less than 1% of total CO<sub>2</sub> in aqueous phase (Table 8) at the end of simulation. The CO<sub>2</sub> gas volume in the reservoir at the end of simulation represented only 0.9-0.15% (Table 11 and 13) of the total pore volume of reservoir (Table 9).

The maximum flow rate during injection was chosen in order to control the average pressure into reservoir and the BHP at the well location. The maximum flow rate during injection in b.i./inlet reservoir was 400 sm<sup>3</sup>/day (Table 12), whereas in tsunami reservoir was 200 sm<sup>3</sup>/day (Table 10). At the reservoir scale, thin reservoirs and caprock are both susceptible to damage by the build-up of pressure during injection, and CO<sub>2</sub> injectivity may be diminished (Ambrose *et al.*, 2008). A similar pressure build-up was observed in all tsunami cases (~30 bars above the initial reservoir pressure). In the b.i./inlet reservoirs, the pressure build-up was also of 30 bars in cases of northern injector well and of 18 bars in cases of southern injector well (InletV5).

The simulation time, including the observation period after injection, varied between 6.5 and 7.5 years for all study cases. According to the trapping mechanism of CO<sub>2</sub> storage and their evolution through time (Fig. 2), at this short period of simulation, the CO<sub>2</sub> is expected to be stored: around 50-60 % by stratigraphic and structural trapping as a mobile gas, 30% by residual trapping also as gas phase, and only 20% by solubility trapping as dissolved in the brine. Here, the amount of CO<sub>2</sub> stored by residual and dissolution trapping was higher than the expected amount.

The distribution of CO<sub>2</sub> into the reservoir, as gas phase or dissolved in the brine, can be influenced by the reservoir heterogeneity. Injection in homogeneous high-permeability zones provides conduits for flow circulation and the lateral distribution of CO<sub>2</sub> in the aqueous phase (Akatsu, 2008; Ambrose *et al.*, 2008; Sifuentes *et al.*, 2009), while heterogeneous permeability zones have reduced injectivity (Hovorka *et al.* 2004; Deng *et al.* 2012), although such zones trap more residual CO<sub>2</sub> (Ambrose *et al.*, 2008, Frykman *et al.* 2013). The heterogeneity of tsunami and b.i./inlet reservoir models is expressed by the contrast of porosity and permeability in the 3D grid. The distribution of permeability and porosity values is strongly correlated with the facies distribution, principally in the b.i./inlet deposit, which were classified as a function of the sand sorting and cemented content. Thus, the spatial distribution of petrophysics values is controlled by the geometry of the depositional facies and the degree of continuity of sand bodies (Ambrose *et al.*, 2008, Veloso *et al.*, 2016).

## 5.1. TSUNAMI RESERVOIR

The distribution of injected CO<sub>2</sub> in the tsunami reservoir was similar in the four study cases. Around 60% of injected CO<sub>2</sub> was stored, with 40% as dissolved in the brine and 20% as residual gas phase. In order to inject a similar quantity of CO<sub>2</sub> in all study cases, the total injection period in cases of different flow rates was around 1.7 years whereas in cases of constant flow rate, it was 4 years (Table 10). The CO<sub>2</sub> as mobile gas phase represented less than 20% of the total CO<sub>2</sub> injected. The similar distribution of CO<sub>2</sub>, independently of the location of injector well or the flow rate, can be linked to the homogenous distribution of porosity (and permeability), described by a normal distribution with a mean of 0.18 and a standard deviation of 0.3 (Fig. 6), and to the homogenous thickness of reservoir (1-3m).

Despite of the similarity of CO<sub>2</sub> distribution, the study cases with the injector well located in the South sector stored more 3% CO<sub>2</sub> as dissolved in brine and residual gas phase (Table 11); in addition, the maximum saturation of gas in the plume at end of simulation is relatively lower (Fig. 19). The cross-sectional view of the tsunami porosity model at well locations (Fig. 22) shows high porosity values (>20%) close to the wellbore in the South sector (Fig. 22A), whereas in the North sector (Fig. 23A) the wellbore is close to lower porosity values (11%–13%). Probably the high porosity-permeability values close to the injector well increased the lateral movement of CO<sub>2</sub> and then increased a little the CO<sub>2</sub> storage.

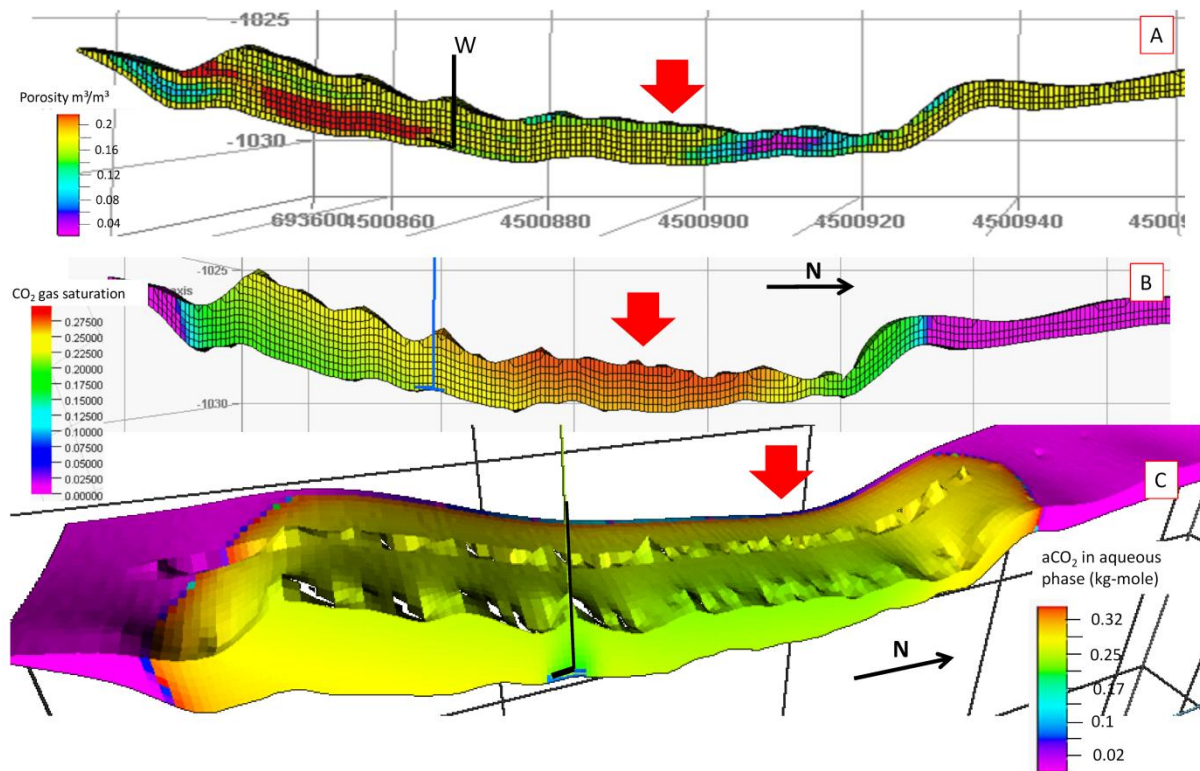


**Fig. 22:** Tsunami reservoir TsunV5 (the injector well in the South sector) at the end of simulation (vertical exaggeration of 4x). The injector well is represented by vertical bars marked 'W' and the red arrow indicates zones of highest gas saturation into the plume. (A) Porosity S-N cross-section at the well location between points 2 and 2' in (Fig. 19B). (B) CO<sub>2</sub> Gas saturation S-N cross-section at

the well location between points 2 and 2' in (Fig. 19B). (C) 3D view of CO<sub>2</sub> activity in aqueous phase with the intersection plan at the well location between points 2 and 2' in (Fig. 19B).

The displacement of CO<sub>2</sub> gas plume and the gas saturation inside the plume could be also related to the location of injector well and the zones of low porosity (<10%). In the layer by layer map view of porosity (Fig. 8), the lower porosity zone close to the injector well is larger and thicker in the North Sector than the South sector. The gas saturation at end of simulation is higher in study cases of North sector, with gas saturation > 0.27 (Fig. 18 and Fig. 23B) whereas in study cases of the South sector gas saturation was <0.27% (Fig. 19 and Fig. 22B). The gas plume moved to the upper parts of reservoir by buoyancy, zones of lower porosity difficult its movement increasing the saturation into the plume. These zones of high gas saturation are correlated with zones of lower activity of CO<sub>2</sub> into the aqueous phase (see red arrow in Fig. 22B – C and 23B - C); probably these zones have more CO<sub>2</sub> as mobile gas phase.

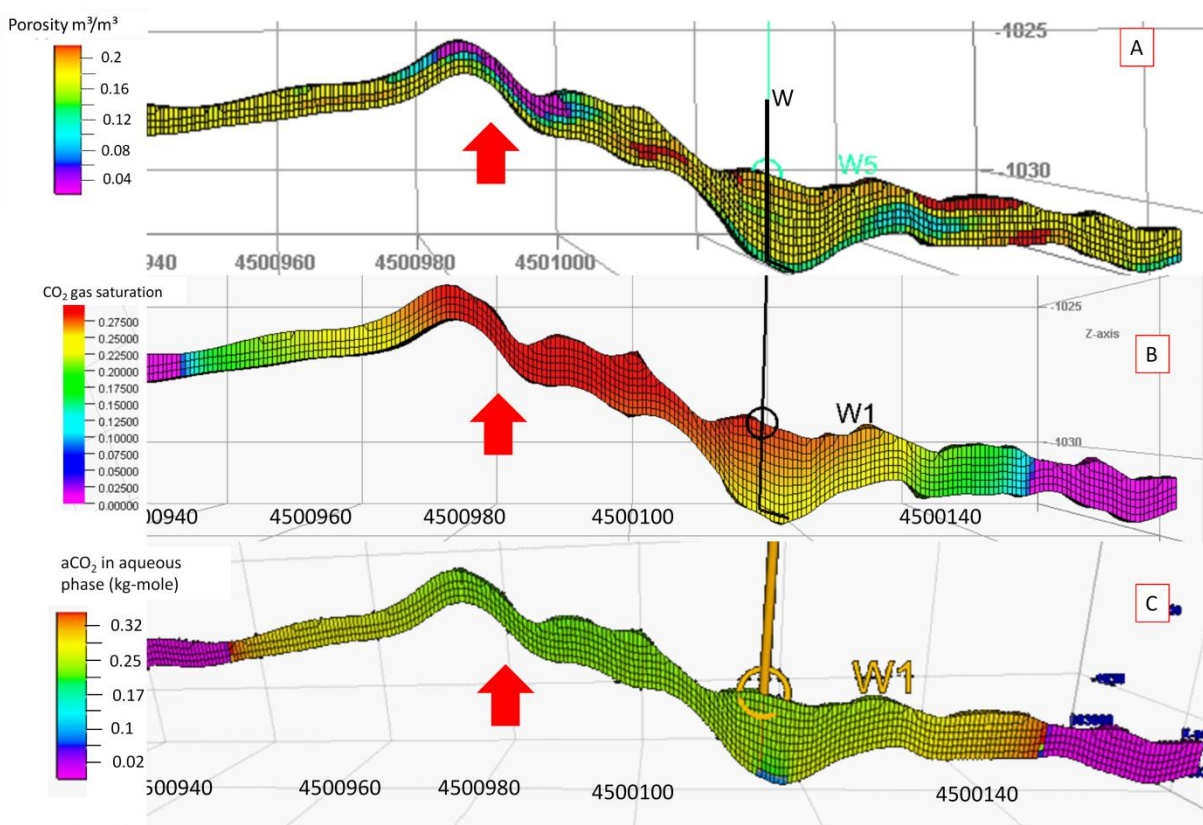


**Fig. 23:** Tsunami model TsunV2 (the injector well in the North sector and vertical exaggeration of 4x). The injector well is represented by vertical bars marked 'W' (A) Porosity S-N cross-section at the well location between points 1 and 1' in (Fig. 18A). (B) CO<sub>2</sub> Gas saturation S-N cross-section at well location between points 1 and 1' in (Fig. 18A). (C) CO<sub>2</sub> activity in aqueous phase S-N cross-section with the intersection plan at the well location between points 1 and 1' in (Fig. 18A).

## 5.2. BARRIER ISLAND – TIDAL INLET RESERVOIR

The b.i./inlet reservoir model is heterogeneous in terms of the porosity and permeability distribution between the North sector with lower permeability  $< 0.5$  (Fig. 24A mD) and the South sector with higher permeability  $> 10$  mD (Fig. 25A), at the well location. The reservoir thickness also is variable at the well location; reservoir thickness up to 7 m (Fig. 21C-D) and 2.2 m (Fig. 20C-D) in the South and North sectors, respectively,.

The higher values of saturation into the plume gas, principally in the case of North sector injector well (Fig. 24B-C), correspond to the zones of less molar  $\text{CO}_2$  activity into the aqueous phase (Fig. 24C). The zone of higher gas saturation into the gas plume in the InletV3 (different flow rates) is larger, and values are higher (up to 0.40) than in InletV4 (constant flow rate), at the end of injection (Fig. 20A-B). In terms of the  $\text{CO}_2$  partitioning in the reservoir, the case InletV3 has around 2% more  $\text{CO}_2$  mobile gas phase than Inlet V4 (Table 13). Although these small differences in the gas plume between cases, both stored around 40% of injected  $\text{CO}_2$  as dissolved in the brine.

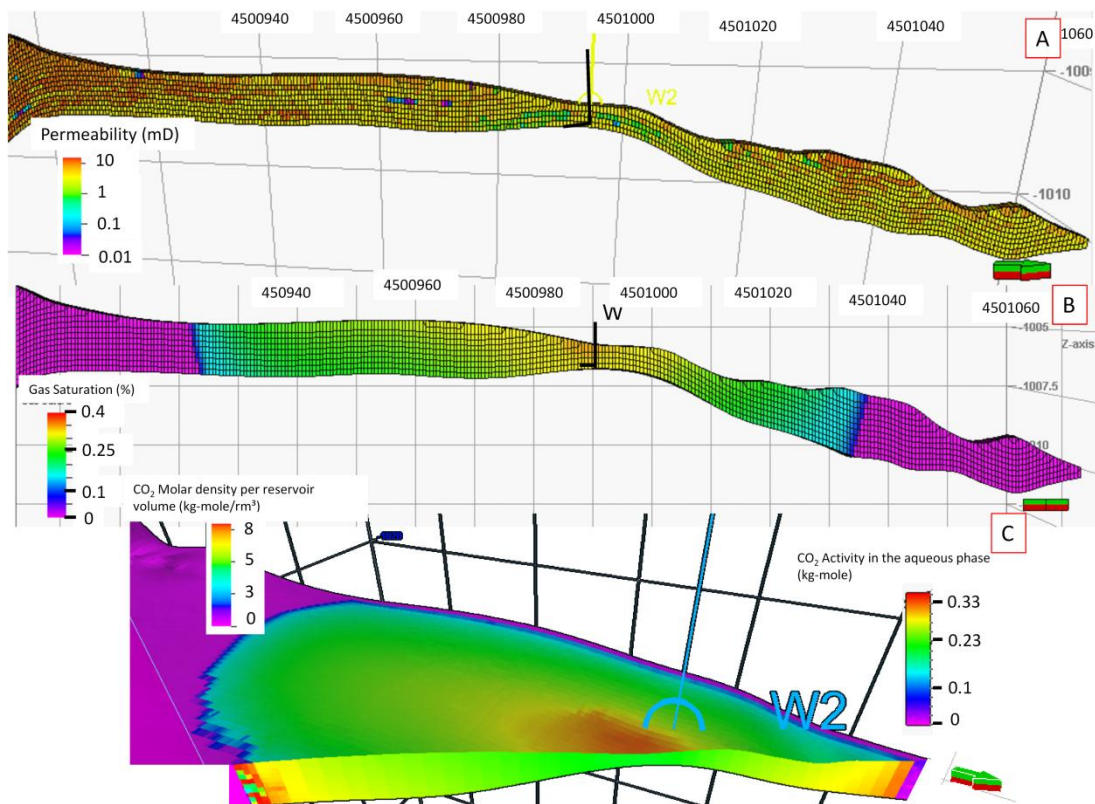


**Fig. 24:** B.i./inlet model InletV3 (the injector well in the North sector and vertical exaggeration of 4x). The injector well is represented by vertical bars marked 'W' (A) Permeability S-N cross-section at the well location between points 1 and 1' in (Fig. 20A). (B)  $\text{CO}_2$  Gas saturation S-N cross-section at well location between points 1 and 1' in (Fig. 20A). (C) 3D view of  $\text{CO}_2$  molar density per reservoir volume.

volume with the intersection plan (IP) representing the CO<sub>2</sub> activity in aqueous phase (see IP location in Fig. 20A).

In the study cases of southern injector well, the saturation into the gas plume is <0.3, and is located above the injector point (Fig. 21B). With regard to molar CO<sub>2</sub> activity into aqueous phase, the concentration is homogenous of around 0.30, as the gas saturation. The displacement and concentration of gas plume is similar between both southern study cases. The case InletV5 (constant flow rate) dissolved slightly more CO<sub>2</sub> (~3%) than InletV6. Although the higher thickness and permeability values in the South sector, the study cases of northern injector well (InletV3 and IV4) stored 20%–25% more CO<sub>2</sub> as dissolved in the brine with 10%–15% less CO<sub>2</sub> as mobile gas phase (Table 13).

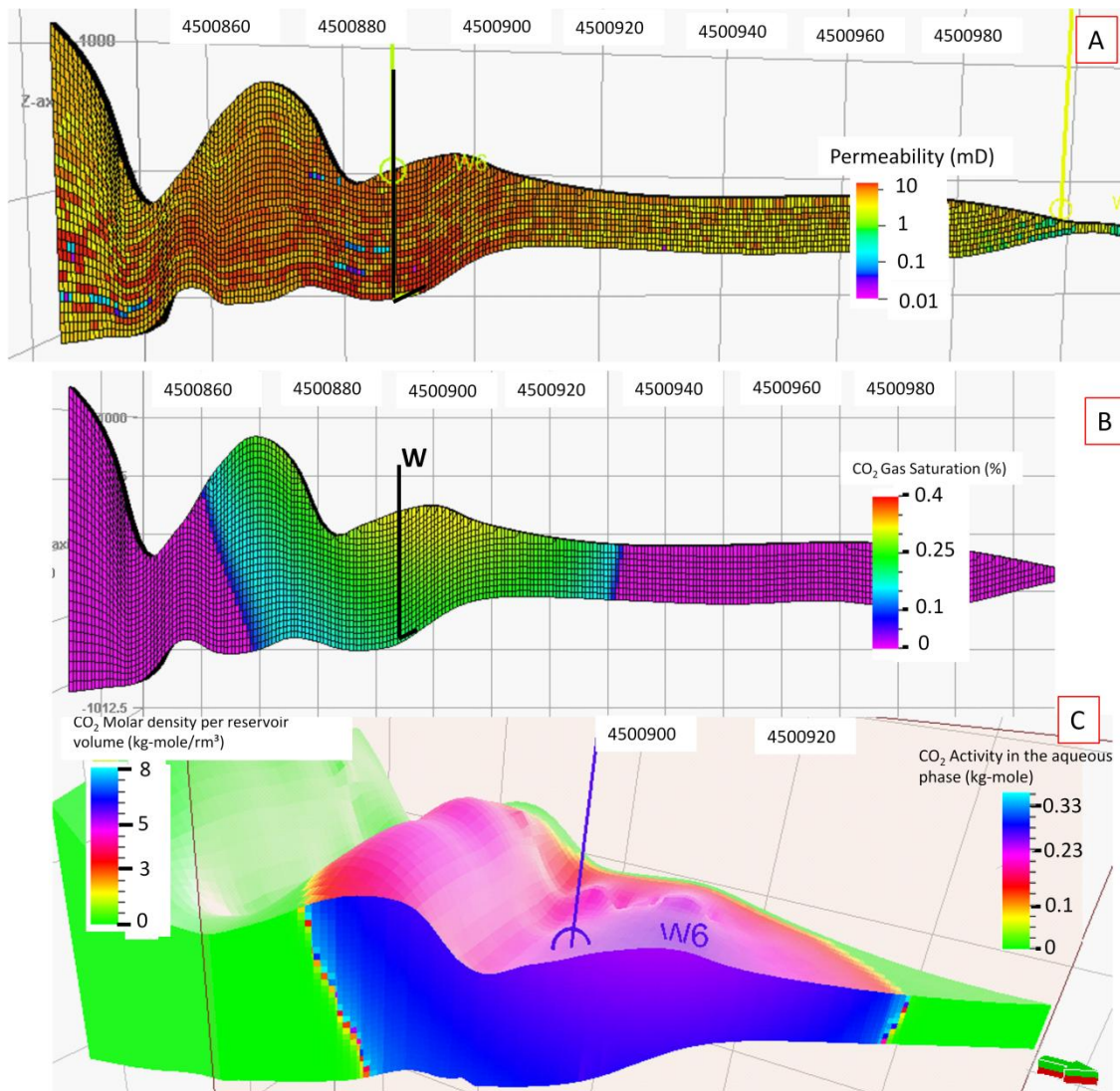


Fig. 25: B.i./inlet model InletV6 (the injector well in the South sector and vertical exaggeration of 4x). The injector well is represented by vertical bars marked 'W' (A) Permeability S-N cross-section at the well location between points 2 and 2' in (Fig. 21B). (B) CO<sub>2</sub> Gas saturation S-N cross-section at well location between points 2 and 2' in (Fig. 21B). (C) 3D view of CO<sub>2</sub> molar density per reservoir

volume with the intersection plan (IP) representing the CO<sub>2</sub> activity in aqueous phase (see IP location in Fig. 21B).

## 6. Conclusion

Despite of the relative low range of permeability values of tsunami and barrier island – tidal inlet reservoirs (0.1–20 mD), both reservoirs stored 50-60% of injected CO<sub>2</sub> by residual and dissolution trapping over 7.5 years. The dissolution of CO<sub>2</sub> reached 40% of total injected CO<sub>2</sub>, where the injection point was in zones of 1–3 m-thick. The cases with the injector well located in zones of 6-7 m-thick, the CO<sub>2</sub> dissolution was 16-19%, as expected in Fig. 2. A constant flow rate slightly improved the CO<sub>2</sub> storage; in cases where the injection was in thicker zones, 4% more CO<sub>2</sub> was stored (residual and dissolution). At the scale of this study (sub-metric), the thickness of reservoir has great impact in the amount of CO<sub>2</sub> dissolution in the zone close to the injector well.

The barrier island – tidal inlet study cases with the injector well in the North sector are the best scenario to inject CO<sub>2</sub>. During the injection period, the limited thickness of reservoir blocked the upward movement of CO<sub>2</sub> and moved it laterally in a restrained volume. The brine, in the restrained volume, is quickly saturated of CO<sub>2</sub>, which increased CO<sub>2</sub> dissolution and accelerated the lateral movement of gas plume. Moreover, the thicker zone of b.i./inlet reservoir dissipated fast the pressure during injection and allowed to inject CO<sub>2</sub> using a flow rate higher than the flow rate used in the tsunami cases.

The injection rate per day, the injection period and the total amount of injected CO<sub>2</sub> (maximum of 116,000 sm<sup>3</sup>, ~200 t) were very low here in comparison with an industrial project; however, some results of this study are useful in studies at reservoir scale, as follows:

- The dissolution of CO<sub>2</sub> can increase significantly with the injection point in thin or below heterogeneous zones of reservoir, such mud drapes. The injection in thinner reservoir zones requires an exhaustive monitoring of the injection rate and pressure build-up to avoid reservoir and top seal damages.

- The comparison of molar distribution of CO<sub>2</sub> activity in aqueous phase and the gas saturation distribution into the plume can help to identify zones of mobile gas phase. The CO<sub>2</sub> as a mobile gas in the reservoir moves upwards and increases the risk of leakage through the top seal. Therefore the monitoring and detection of zones with mobile gas phase is fundamental during and after injection of CO<sub>2</sub>.

## Acknowledge

This research is a contribution to the project: 'Análisis de Cuencas Sedimentarias Continentales', of the Gobierno de Aragón, the Analisis de Cuencas Sedimentarias Group of the UCM-CAM, and the projects CGL2011-23717 (Ministerio de Ciencia e Innovacion of the Spanish Government and FEDER) and UZ2015-CIE-10 (University of Zaragoza). Additional

financial support was provided by a CNPq (Conselho Nacional de Pesquisa e Desenvolvimento Tecnológico, Brasil) Research Grant (200147/2011-0) to F.M.L. Veloso. We are also grateful to Patrice Creux of UPPA (Université de Pau et des Pays de l'Adour, France) for receiving F.M.L. Veloso during her PhD in the LFCR (Laboratoire des Fluides Complexes et leurs Réservoirs), and assistance with the early phase of modelling and simulation of this study.

## References

- Akaku, K., 2008. Numerical Simulation of CO<sub>2</sub> Storage in Aquifers without Trapping Structures. International Petroleum Technology Conference, 3-5 December, Kuala Lumpur, Malaysia. IPTC-12304-MS.
- Ambrose, W.A., Lakshminarasimhan, S., Holtz, M.H., Núñez-López, V., Hovorka, S.D., Duncan, I., 2008. Geologic factors controlling CO<sub>2</sub> storage capacity and permanence: case studies based on experience with heterogeneity in oil and gas reservoirs applied to CO<sub>2</sub> storage. *Environmental Geology* 54, 1619–1633.
- Boxiao, L., Tchelepi, H.A., Benson, S.M. 2013. The Influence of Capillary Entry-Pressure Representation on CO<sub>2</sub> Solubility Trapping. *Energy Procedia* 37, 3808 – 3815.
- Celia, M.A., Bachu, S., Nordbotten, J.M., Gasda, S.E, Dahle, H.K., 2005. Quantitative estimation of CO<sub>2</sub> leakage from geological storage: analytical models, numerical models, and data needs. *Greenhouse Gas Control Technologies* 7, 1, 663-671.
- Chadwick, A., Arts, R., Bernstone, C., May, F., Thibeau, S., Zweigel, P., 2008 - Best practice for the storage of CO<sub>2</sub> in saline aquifers. British Geological Survey, Occasional Publication 14, 277 p.
- Chang, C., Zhou, Q., Guo, J., Yu, Q., 2014. Supercritical CO<sub>2</sub> dissolution and mass transfer in low-permeability sandstone: Effect of concentration difference in water-flood experiments. *International Journal of Greenhouse Gas Control* 28, 328–342.
- Corey, A.T., 1954. The interrelation between gas and oil relative permeabilities. *Producers Monthly* 19 (November): 38–41.
- Deng, H., Stauffer, P.H., Dai, Z., Jiao, Z., Surdam, R.C., 2012. Simulation of industrial-scale CO<sub>2</sub> storage: Multi-scale heterogeneity and its impacts on storage capacity, injectivity and leakage. *International Journal of Greenhouse Gas Control* 10, 397-418.
- Doughty, C., 2007. Modeling geologic storage of carbon dioxide: Comparison of non-hysteretic and hysteretic characteristic curves. *Energy Conversion and Management* 48, 1768–1781.
- EEA – (European Environment Agency), 2014. Annual European Union greenhouse gas inventory 1990–2012 and inventory report 2014. Technical report No 09/2014.

EU, 2009. European Parliament and of the Council Directive 2009/31/EC on the geological storage of carbon dioxide and amending Council Directive 85/337/EEC, European Parliament and Council Directives 2000/60/EC, 2001/80/EC, 2004/35/EC, 2006/12/EC, 2008/1/EC and Regulation (EC) No 1013/2006.

Fenghour, A., Wakeham, W.A., and Vesovic, V., 1998. The Viscosity of Carbon Dioxide. *Journal of Physical and Chemical Reference Data* 27, 1, 31-44.

Frykman, P., 2009. The importance of geological heterogeneities. CO2GeoNet Open Forum March 18-20, Venice, San Servolo Island, Italy.

Frykman, F., Nielsen, C.M., Bech, N., 2013. Trapping effects of small scale sedimentary heterogeneities. *Energy Procedia* 37, 5352 – 5359.

Green, C., Ennis-King, J., Pruess, K., 2009. Effect of Vertical Heterogeneity on Long-Term Migration of CO<sub>2</sub> in Saline Formations. *Energy Procedia* 1, 1823–1830.

Hovorka, S.D., Doughty, C., Benson, S.M., Pruess, K., Knox P.R., 2004. The impact of geological heterogeneity on CO<sub>2</sub> storage in brine formations: a case study from the Texas Gulf Coast. In: Baines S.J., Worden R.H. (eds), *Geological storage of carbon dioxide*. Geological Society of London Special Publication 233, 147–163.

IAPWS (The International Association for the Properties of Water and Steam), 1997. *Industrial Formulation 1997 for the Thermodynamic Properties of Water and Steam*.

IEA-GHG (IEA Greenhouse Gas R&D Programme), 2009. Summary report of 1st IEA-GHG CO<sub>2</sub> Geological Storage Modelling Network Meeting. BRGM, Orleans, France. [http://ieaghg.org/docs/Modelling/2009-5\\_Summary.pdf](http://ieaghg.org/docs/Modelling/2009-5_Summary.pdf).

IFP (Instituto Petrofísico de Madrid), 2012. Helium Porosity and Permeability measurements. Technical Report.

IPCC (Intergovernmental Panel on Climate Change), 2005. *IPCC Special Report on Carbon Dioxide Capture and Storage*. Cambridge University Press, New York. 431 p.

Juanes, R., Spiteri, E.J., Blunt, M.J., 2006. Impact of relative permeability hysteresis on geological CO<sub>2</sub> storage. *Water Resources Research*, 42, W12418, doi:10.1029/2005WR004806.

Navarrete, R., 2015. Controles alocíclicos de la sedimentación barremiense en la Subcuenca de Galve (Fm. Camarillas, margen occidental de la Cuenca del Maestrazgo). PhD Thesis, Univ. de Zaragoza. 444 p.

Navarrete, R., Rodríguez-López, J.P., Liesa, C.L., Soria, A.R., Veloso, F.M., 2013. Changing physiography of rift basins as a control on the evolution of mixed siliciclastic–carbonate back-barrier systems (Barremian Iberian Basin, Spain). *Sedimentary Geology* 289, 40–61.

Navarrete, R., Liesa C.L., Castanera D., Soria, A.R, Rodríguez-López, J.P., Canudo, J.L., 2014. A thick Tethyan multi-bed tsunami deposit preserving a dinosaur megatracksite within a coastal lagoon (Barremian, eastern Spain). *Sedimentary Geology* 313, 105–127.

- Nomeli, M.A., Tilton, N., Riaz, A., 2014. A new model for the density of saturated solutions of CO<sub>2</sub>-H<sub>2</sub>O-NaCl saline aquifers. *International Journal of Greenhouse Gas Control* 31, 192–204.
- Nordbotten, J.M., Celia, M.A., Bachu, S., 2005. Injection and storage of CO<sub>2</sub> in deep saline aquifers: Analytical solution for CO<sub>2</sub> plume evolution during injection. *Transport in Porous Media* 58, 339–360.
- Pettijohn, F.J., Potter, P.E., Siever, R., 1973. *Sand and sandstone*. Springer-Verlag, New York-Heidelberg-Berlin, 618 p.
- Pini, R., Krevor, S.C.M., Benson, S.M., 2012. Capillary pressure and heterogeneity for the CO<sub>2</sub>/water system in sandstone rocks at reservoir conditions. *Advances in Water Resources* 38, 48–59.
- Plug, W.J., Bruining, J., 2007. Capillary pressure for the sand-CO<sub>2</sub>-water system under various pressure conditions. Application to CO<sub>2</sub> sequestration. *Advances in Water Resources* 30, 2339–2353.
- Prost, P., 2008. Numerical Simulations of CO<sub>2</sub> Injection into Saline aquifers: estimation of storage capacity and arrival times using multiple realizations of heterogeneous permeability fields. PhD Thesis, University of Stuttgart, Germany, 69 p.
- Pyrzcz, M. J., Deutsch, C.V. 2014. *Geostatistical reservoir modeling*. Oxford university press, 448 p.
- Schlumberger, 2013a. *Eclipse Technical Descriptions, Version 2013.1*, 58 p.
- Sifuentes, W.F., Giddins, M.A., Blunt, J.B., 2009. Modeling CO<sub>2</sub> Storage in Aquifers: Assessing the key contributors to uncertainty. SPE 123582. <http://dx.doi.org/10.2118/123582-MS>.
- Spiteri, E., Juanes, R., 2006. Impact of relative permeability hysteresis on the numerical simulation of WAG injection. *Journal of Petroleum Science and Engineering* 50, 115–139.
- Spycher, N., Pruess, K., 2005. CO<sub>2</sub>-H<sub>2</sub>O mixtures in the geological sequestration of CO<sub>2</sub> II. Partitioning in chloride brines at 12-100 C and up to 600 bar. *Geochimica et Cosmochimica Acta* 69, 13, 3309-3320.
- Spycher, N., Pruess, K., Ennis-King, J., 2003. CO<sub>2</sub>-H<sub>2</sub>O mixtures in the geological sequestration of CO<sub>2</sub>. I. Assessment and calculation of mutual solubilities from 12 to 100°C and up to 600 bar. *Geochimica et Cosmochimica Acta* 67, 16, 3015–3031.
- Veloso, F.M.L., 2015. *3D Dynamic Modelling of Cretaceous Sandstones at the Outcrop Scale (Galve Subbasin, Iberian Basin). Application to Studies of CO<sub>2</sub> Injection*. PhD thesis. Univ. de Zaragoza, p. 204.
- Veloso, F.M.L., Navarrete, R., Soria, A.R., Meléndez Hevia, M.N., 2013. Estudio de afloramiento de escala intermedia como almacén geológico (Aliaga, provincia de Teruel). In: Garcia-Hidalgo, J.F., Gil, Barroso, F., Diaz de Neira, J.A. (eds), V Congreso Cretácico de España, 136-139.

Veloso, F.M.L., Navarrete, R., Soria, A.R., Meléndez, N., 2016. Sedimentary heterogeneity and petrophysical characterization of Barremian tsunami and barrier island/inlet deposits: The Aliaga outcrop as a reservoir analogue (Galve sub-basin, eastern Spain). *Marine and Petroleum Geology*, 73, 188-211.

Vogel, W. CO<sub>2</sub> sequestration simulations: A comparison study between DuMuX and Eclipse. PhD thesis, Univ. of Stuttgart, p.100.

Vesovic, V., Wakeham, W. A., Olchoway, G.A., Sengers, J.V., Watson, J.T.R., Millat, J., 1990. The Transport Properties of Carbon Dioxide. *Journal of Physical and Chemical Reference Data* 19, 3, 763.

Zaytsev, I.D., Aseyev, G.G., 1993. *Properties of Aqueous Solutions of Electrolytes*. Boca Raton, Florida, USA CRC